学位論文

光周波数コムの光/電気周波数変換を用いた屈折率センシングに関する研究

2021 年 9 月

麻植 凌

PhD thesis

Study on refractive index sensing based on optical-to-electric frequency conversion in optical frequency comb

September, 2021

Ryo Oe

Contents

1. Introduction

Refractive index (RI) is defined as a ratio of the speed of light in vacuum to the phase velocity of light in the medium. In other words, RI is an inherent physical quantity that describes how fast light travels through the material. Since RI is derived from the permittivity peculiar to a substance and hence represents the interaction between light and a substance, RI sensing can be used for quality evaluation of liquid substances and characteristic evaluation of optical components.

Various methods for RI sensing have been proposed. For example, in the minimum argument method [1], when the light is incident into a prism-shaped sample, the deflection angle of the transmitted light is measured; typical RI resolution is ~ 1×10^{-5}. The critical angle method [1] is a method of measuring the RI by using the total reflection occurring at the interface between the prism and the sample; typical RI resolution is ~ 1×10^{-4}. The V-block method [1] is a method of determining RI of a sample placed on a V-shaped prism by measuring the refraction angle of the light passing through the prism and the sample; typical RI resolution is ~ 2×10^{-5}. The surface plasmon resonance (SPR) method [2] is a method of measuring the spectral or angle shift of SPR dip when a sample is put onto a gold thin film deposited on a prism; typical RI resolution is ~ 1×10^{-5}. These conventional methods can be classified into the measurement of the change in light intensity at a fixed wavelength and the measurement of the wavelength shift of the optical spectrum peak. However, the RI resolution of them is remained around the order of 10^{-4} to 10^{-5} depending on the performance of the measuring instrumentation. In order to improve quality control in the industrial field, further high accuracy and high resolution are required. Also, there is a considerable need for RI sensing with high versatility and practicality.

The fiber-based RI sensor is a powerful means for RI measurement because of its

compactness, simplicity, flexibility, noise robustness and availability in various environments and has been applied in many applications in sucrose sensing [3], gas pressure sensing [4] and biomolecule sensing [5]. In the conventional RI fiber sensors, which are based, for example, on SPR [6], interference with a core-offset fiber [7], or multimode interference (MMI) [8], the change of RI is measured by a shift of transmitted optical spectrum. However, the sensitivity of the conventional RI sensing is limited due to the relatively broad bandwidth of a spectral dip (or peak) and spectral resolution of a spectrometer.

If a change in the RI of a sample is transformed into a photonic radio-frequency (RF) signal, the RI sensing benefits from high-precision, high functionality, convenience, and low cost by making use of frequency standards and precise measurement apparatuses in the RF region. Such photonic RF fiber sensors based on radio-frequency (RF) signal measurement have been effectively applied for strain sensing [9] and ultrasound sensing [10, 11] by using multiple-longitudinal-mode or multiple-polarization-mode spacing in a continuous-wave (CW) fiber laser or a CW fiber-Bragg-grating laser. However, the inherent frequency fluctuation of mode spacing hampers high-precision RI sensing.

Recently, an optical frequency comb (OFC) [12-14] appeared as a new photonic RF converter. OFC is regarded as a group of a vast number of phase-locked narrow-linewidth continuous-wave (CW) light sources with a constant frequency spacing f_{rep} (typically, 50–100 MHz) over a broad spectral range. The inherent mode-locking nature and active laser control enable us to use an OFC as an optical frequency ruler traceable to a microwave or RF frequency standard. Based on the concept of an optical frequency ruler, OFCs have found many applications in optical frequency metrology and distance metrology; examples include atomic spectroscopy [13], gas spectroscopy [15], solid spectroscopy [16], spectroscopic ellipsometry [17], strain sensing [18], and distance measurement [19]. Also, time characteristics of OFC has been applied for the ultrafast spectroscopy by the help of asynchronous optical sampling [20,

21]; for example, detection of coherent phenomena [22, 23] and relaxation dynamics of saturable absorber [24].

Another interesting feature of OFCs is a coherent link between the optical and radio frequencies. For example, when an OFC is detected with a photodiode, its quadratic-detection function converts a mode spacing of OFC into a beat signal in the RF region without changing f_{rep}. While the mode spacing of the OFC is transferred into the RF beat signal via such a coherent detection process, use of the RF beat signal simplifies the experimental methodology because measurement in the RF region benefits from high precision, high functionality, convenience, and low cost by making use of various kinds of RF measurement apparatuses. Therefore, the RF beat signal and its harmonic components have been applied to optical distance metrology, such as long-distance measurement with extremely high precision [25-27].

Recently, a fiber OFC has been further used for a photonic RF fiber sensor for strain [28], acoustic wave [29] and ultrasound sensing [30]. The key feature required to enable this new use of OFC is a photonic RF conversion function in a fiber OFC cavity. The repetition frequency f_{rep} in a ring cavity is given by

$$f_{rep} = \frac{c}{nL}, \tag{1}$$

where c is the speed of light in vacuum, n is a refractive index of a cavity fiber, L is a geometrical length of a fiber cavity. If external disturbance, such as temperature change, strain, or vibration, is interacted with the fiber OFC cavity, f_{rep} shifts as a result of change of the optical path length nL. In other words, OFC can act as a photonic RF converter for external disturbance. Since RF frequency measurement can be performed with high precision and wide dynamic range due to excellent frequency standards, the combination of the photonic RF converter with RF frequency measurement, namely photonic RF sensor, has a potential to largely enhance precision and dynamic range over conventional electric or photonic sensors. However, when a single-mode fiber in the cavity is used as a sensor, a measurable sensing quantity is limited to

physical quantity that directly interacts with the fiber OFC cavity, such as strain [28], acoustic pressure [29], or ultrasound waves [30].

Photonic RF sensors that can sense a wide variety of physical quantities will become possible if a functional fiber sensor can be introduced into a fiber OFC cavity. Such intracavity fiber sensors will benefit from the sensitivity enhancement made possible by the multiple passages of light thorough the sensors in addition to photonic RF conversion. One interesting application of photonic RF sensors is in RI sensing. If high-precision RF measurement can be used for the optical RI sensing, its sensing precision will be largely enhanced.

In this PhD thesis, we combined the fiber OFC cavity with a multi-mode interference (MMI) fiber sensor for RI measurement [31-33]. An MMI fiber sensor is composed of a clad-less multi-mode fiber (MMF) with a pair of SMFs at the two ends, has good compatibility with fiber OFC cavities, and works as an RI sensor based on a change in MMI wavelength λ_{MMI} due to the Goos-Hänchen shift on the surface of the clad-less MMF. An RI-dependent shift of λ_{MMI} in the fiber OFC cavity is converted into a shift of f_{rep} via wavelength dispersion of the cavity fiber. To this end, we introduced an MMI fiber sensor into a fiber OFC cavity, forming what we call an MMI-OFC, and read out the change in RI in a sample solution via f_{rep} to demonstrate the potential of MMI-OFCs as photonic RF sensors for RI.

This PhD thesis is organized by the following three topics.

(1) Refractive-index-sensing optical comb based on photonic radio-frequency conversion with intracavity multi-mode interference fiber sensor [34]

(2) Improvement of dynamic range and repeatability in a refractive-index-sensing optical comb by combining saturable-absorber-mirror mode-locking with an intracavity multimode interference fiber sensor [35]

(3) Refractive index sensing with temperature compensation by a multimode-interference fiber-based optical frequency comb sensing cavity [36]

In the first topic of this PhD thesis, for proof of concept in RI sensing MMI-OFC, we integrated an MMI fiber sensor into a fiber OFC for f_{rep}-based RI measurement. By using the OFC was used here as a photonic RF converter, the sample RI is converted into an OFC mode spacing f_{rep} via a combination of RI-dependent tunable bandpass filtering by an intracavity MMI fiber sensor and wavelength dispersion by a cavity fiber. Due to the ultranarrow linewidth and high stability in the mode-locking oscillation, this MMI-OFC enables us to precisely measure the RI-dependent f_{rep} shift by using an RF frequency counter synchronized with a rubidium frequency standard. Combined use of the MMI-OFC with high-precision RF measurement enables us to enhance a resolution and an accuracy in RI sensing.

In the second topic of this PhD thesis, we improved the MMI-OFC to enhance the dynamic range and the repeatability in RI sensing. Notable problems with the previous MMI-OFC include its limited dynamic range and the low repeatability of RI sensing, which are caused by the nonlinear-polarization rotation (NPR) [37] used for mode-locking oscillation in the MMI-OFC. Although NPR has been widely used for the fiber-based OFC with broad optical bandwidth, it is less robust against external disturbance to the cavity because of high sensitivity to the fiber birefringence. In the MMI- OFC, a large change in the sample RI causes a change in the intracavity polarization condition via the intracavity MMI fiber sensor, leading to a nonnegligible disturbance to the cavity and the disruption of mode-locking oscillation. This is the reason for the limited dynamic range of RI sensing. On the other hand, NPR-based mode-locking oscillation is activated by polarization adjustment in the fiber cavity with a polarization controller. While such polarization adjustment enables flexible mode-locking oscillation, f_{rep} changes with every mode-locking activation, leading to low repeatability. If high repeatability of f_{rep} can be achieved in an RI sensing MMI-OFC, the RI sensing repeatability will be enhanced. To overcome the limited dynamic range and the low repeatability of RI sensing, a robust mode-locking mechanism with fewer degrees of freedom is required in the RI sensing

MMI-OFC. One possible candidate for such a purpose is mode-locking oscillation with a saturable-absorber mirror (SAM) [38]. SAM enables easy, stable, and robust mode-locking oscillation without the need for polarization control. While such characteristics in SAM enable us to expand the dynamic range of RI sensing in MMI-OFC, mode-locking oscillation with fewer degrees of freedom will contribute to obtaining high repeatability for both f_{rep} and RI sensing. To this end, we evaluate the validity of SAM- based MMI-OFC (SAM-MMI-OFC) by comparing it with the previous NPR-based MMI-OFC (NPR-MMI-OFC).

In the third topic of PhD thesis, to improve the RI measurement with the MMI-OFC sensing cavity in the condition of fluctuated sample temperature, we realized simultaneous measurement of temperature with the same configuration of MMI-OFC-sensing cavity for RI measurement by simultaneous monitoring of an optical spectral shift in the optical frequency region and a comb spacing shift in the RF region of the OFC. Although the highly sensitive RI measurement was realized based on the MMI-OFC sensing cavity, further improvements of the sensitivity and stability of RI measurement was expected if the sample temperature fluctuation was stabilized or monitored. This is because the RI of a sample is dependent on the temperature of the sample, and the instability of the fiber structure at the sensing region due to temperature fluctuations led to the instability of RI measurement with the MMI-OFC sensing cavity. We confirmed the fundamental sensitivity of the MMI-OFC sensing cavity depending on sample temperature and RI-related concentration of a liquid sample. Furthermore, we demonstrated simultaneous and continuous measurement of temperature and RI-related concentration of a liquid sample.

2. Refractive-index-sensing optical comb based on photonic radio-frequency conversion with intracavity multi-mode interference fiber sensor

2.1 Materials and methods

2.1.1 Principle of operation

A schematic diagram of the MMI fiber sensor is shown in Fig. 1(a). Broadband light passing through the input SMF is diffracted at the entrance face of the clad-less MMF, and then repeats total internal reflection at the boundary between the clad-less MMF surface and the sample solution (typical number of reflections: a few tens to a few hundreds). When a light beam undergoes total internal reflection in the clad-less MMF, the beam is spatially shifted as if it had briefly penetrated the surface before bouncing back (Goos-Hänchen shift), as shown in an inset of Fig. 1(a). The penetration Z is given by [39]

$$Z = \frac{\lambda / n_{MMF}}{2\pi\sqrt{\sin^2\theta - \left(n_{sam} / n_{MMF}\right)^2}}, \tag{2}$$

where λ is the wavelength of transmitting light, n_{MMF} is the refractive index of the clad-less MMF, θ is the incident angle of the light to the cladding, and n_{sam} is the sample RI. When the order of the MMI, m, is equal to 4, all modes of light are refocused as shown in Fig. 1(a), and the constructive interference of light has the maximum peak intensity at the MMI wavelength λ_{MMI} [39]. λ_{MMI} light mainly exits through the clad-less MMF and then goes toward the output SMF. λ_{MMI} is given by [40]

$$\lambda_{MMI} = \frac{n_{MMF} m}{L_{MMF}} \left[D\left(n_{sam}\right) \right]^2 , \tag{3}$$

where L_{MMF} is the geometrical length of the clad-less MMF and $D(n_{sam})$ is the effective diameter of the clad-less MMF influenced by the Goos-Hänchen shift [see an inset of Fig. 1(a)]. From Eqs. (2) and (3), when n_{sam} changes, Z and the corresponding $D(n_{sam})$ change; therefore, λ_{MMI} is a function of n_{sam}. Since the intracavity MMI fiber sensor also receives the similar effect, the MMI-OFC output light shows the RI-dependent shift of optical spectrum. Such RI-dependent optical-spectrum shift experiences the wavelength dispersion of the cavity fiber rather than the intracavity MMI fiber sensor. In other words, the change of nL in Eq. (1), caused by the RI-dependent optical-spectrum shift, leads to the RI-dependent f_{rep} shift. Within the limited range of the sample RI, this RI-dependent f_{rep} shift can be linearized as demonstrated later.

The MMI fiber sensor was composed of a clad-less MMF (core diameter = 125 μm, fiber length = 58 mm) with a pair of SMFs at both ends (core diameter= 6 μm, clad diameter = 125 μm, fiber length = 54 mm), in which the diameter of the SMF clad was equal to that of the clad-less MMF core. In the present MMI-OFC, we set m to 4 for use of the intracavity MMI fiber sensor as the RI-dependent tunable band-pass filter. Due to the spectral bandpass-filtering effect in the MMI process, the MMI fiber sensor acts as an RI sensor showing an RI-dependent λ_{MMI} shift. We designed the parameters of the MMI fiber sensor so that the spectral peak appeared around the center wavelength of fiber OFC (= 1555 nm) when the sample is a pure water sample (0 EtOH%, RI = 1.333 refractive index units or RIU).

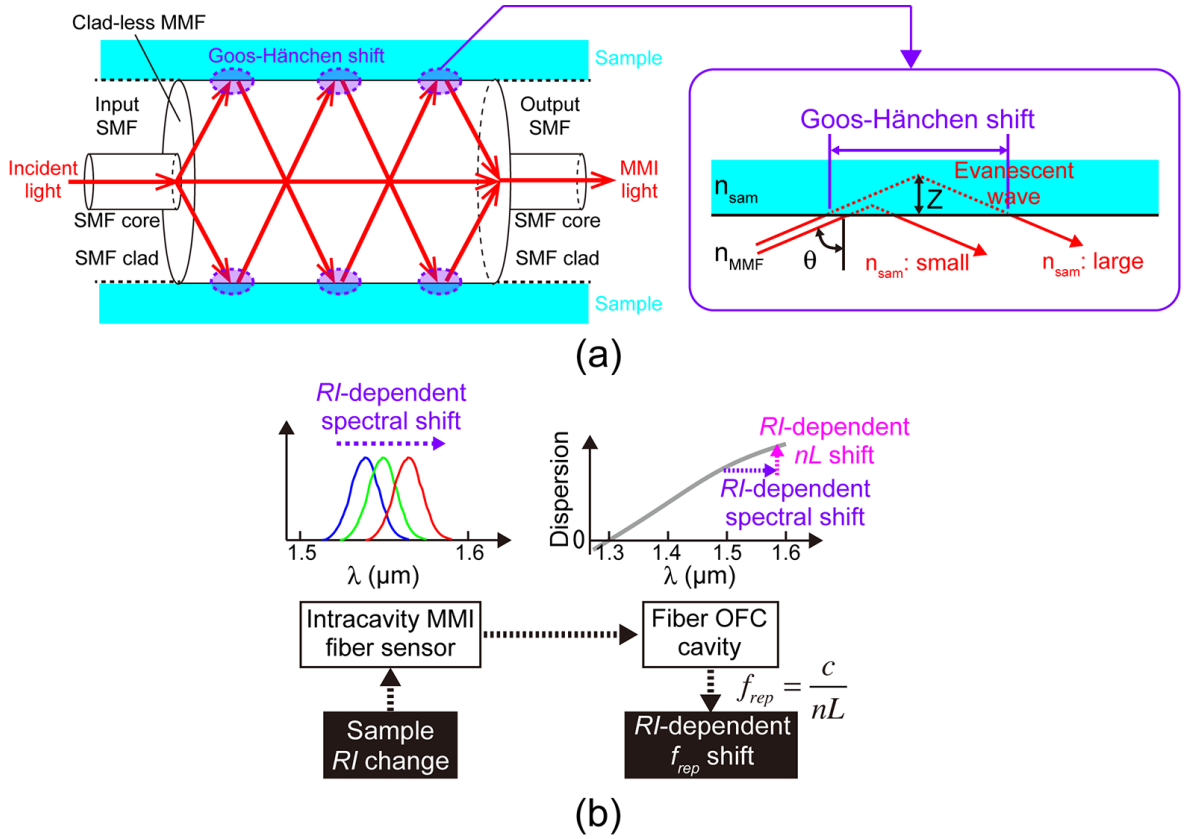

Fig. 1. Principle of operation. (a) Schematic diagram of the MMI fiber sensor. An inset of Fig. 1(a) shows a schematic drawing of the Goos-Hänchen shift on the surface of the clad-less MMF. The MMI fiber sensor functions as an RI-dependent tunable bandpass filter via the MMI process. (b) Conversion from sample RI change to RI-dependent f_{rep} shift. The intracavity MMI fiber sensor shifts the optical spectrum of the MMI-OFC depending on the sample RI. The wavelength-shifted MMI-OFC spectrum experiences the wavelength dispersion of the cavity fiber, resulting in the conversion from an RI-dependent spectral shift to an RI-dependent shift of the optical cavity length nL. Such an RI-dependent nL shift leads to an RI-dependent f_{rep} shift based on Eq. (1).

2.1.2 MMI fiber sensor

We used a mode-locked Er:fiber laser oscillator for the MMI-OFC (see Fig. 2). This oscillator had a ring cavity including a 2.9 m length of single-mode fiber (SMF, SMF-28, Corning, dispersion at 1550 nm = 17 ps/km/nm), a 1.6 m length of erbium-doped fiber (EDF, ER30-4/125, LIEKKI, dispersion at 1550 nm = -15 ps/km/nm), a polarization controller [PC, PCUA-15-S/F(15P/15Q/15H), Optoquest Co., Ltd.], a polarization-insensitive isolator (ISO, PSSI-55-P-I-N-B-I, AFR), a 70:30 fiber coupler (FC, SBC-1-55-30-1-B-1, AFR), a wavelength-division-multiplexing coupler (WDM, WDM-1-9855-1-L-1-F, AFR), and a pumping laser

diode (LD, BL976-PAG900, Thorlabs, wavelength = 980 nm, power = 900 mW). The temperature of the fiber cavity was controlled to 25.0ºC by a combination of a Peltier heater (TEC1-12708, Kaito Denshi, power = 76 W), a thermistor (PB7-42H-K1, Yamaki), and a temperature controller (TED200, Thorlabs, PID control). Stable soliton mode-locking oscillation was achieved by nonlinear polarization rotation with near zero cavity dispersion (= -0.045 pm/s^2) before and after introducing the MMI fiber sensor in the cavity. The output light from the oscillator was detected by a photodetector (PD), and its f_{rep} was measured by an RF frequency counter (53230A, Keysight Technologies, frequency resolution = 12 digit/s) and an RF spectrum analyzer (E4402B, Keysight Technologies, frequency resolution = 1 Hz), both of which were synchronized to a rubidium frequency standard (FS725, Stanford Research Systems, accuracy = 5×10^{-11} and instability = 2×10^{-11} at 1 s). Also, its optical spectrum was measured by an optical spectrum analyzer (AQ6315A, Yokogawa Electric Corp., wavelength accuracy = 0.05 nm, wavelength resolution = 0.05 nm).

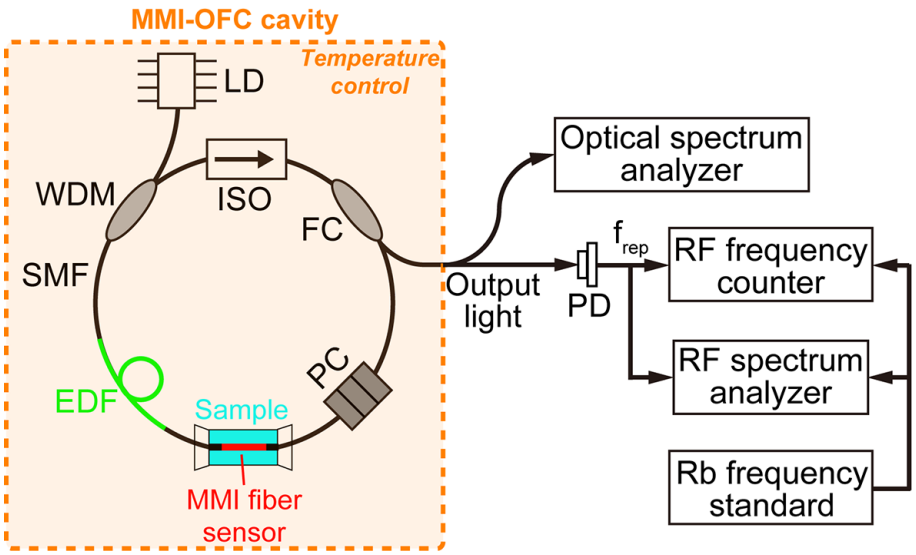

Fig. 2. Experimental setup. See Materials and methods for details.

2.1.3 Samples

Mixtures of ethanol and pure water were used as standard samples. The sample RI was adjusted by changing the mixture ratio between ethanol and water. The relationship between the ethanol concentration *EC* (unit: EtOH%) and the sample RI (unit: RIU) is given by [41]

$$RI = 1.3326 + 4.90 \times 10^{-4} \times EC. \quad (4)$$

The temperature of the sample was controlled to 22ºC by a combination of a K-type thermocouple (TJA-550K, AS ONE), a cord heater (603-60-69-01, Tokyo Glass Kikai, power = 15 W), and a temperature controller (TJA-550, AS ONE, PID control, display resolution = 0.1ºC).

2.2 Results

2.2.1 Basic characteristics of fiber OFC

Stable mode-locking oscillation in the MMI-OFC is indispensable for high-precision RI sensing. Here we compare an optical spectrum of the MMI-OFC with that of a usual OFC. The blue line in Fig. 3 shows an optical spectrum of a usual OFC (center wavelength = 1561.8 nm, spectral bandwidth = 15 nm, mean power = 4.7 mW), indicating the symmetrical broad spectrum, together with some spikes due to the soliton mode-locking oscillation near the zero-dispersion region of the cavity (-0.045 pm/s^2). On the other hand, the red line in Fig. 3.4 shows an optical spectrum of an MMI-OFC. The spectral bandpass-filtering effect of the intracavity MMI fiber sensor decreased the spectral bandwidth and the mean power to 10 nm and 2.9 mW, respectively. In this way, we could obtain stable mode-locking oscillation even in the MMI-OFC.

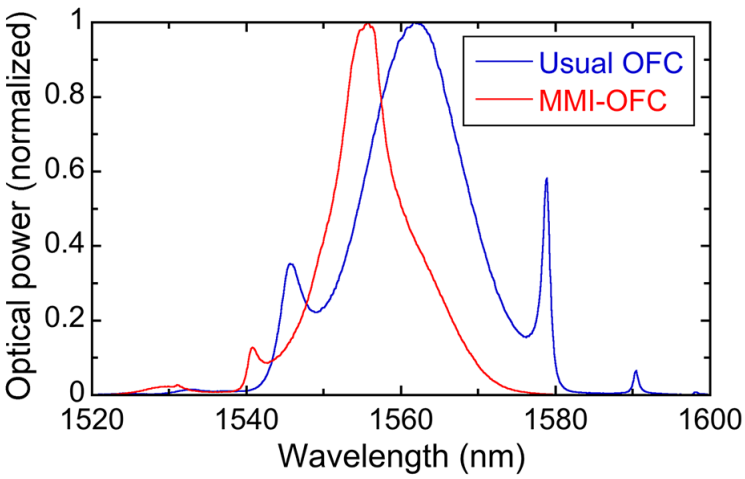

Fig. 3. Comparison of optical spectrum between usual OFC and MMI-OFC.

Next, we investigate RF spectra of the MMI-OFC light because the multi-mode propagation and polarization spread in the intracavity MMI fiber sensor may superimpose unnecessary parasitic side modes on the RF beat signal. Figure 4(a) shows the RF spectrum of the MMI-OFC light within the frequency range of 0 to 3000 GHz when the resolution bandwidth (RBW) and the video resolution bandwidth (VBW) were set to 300 kHz. The fundamental component and 68 harmonic components of repetition frequency appeared as frequency spikes with a constant frequency spacing of f_{rep}, namely RF com modes; however, no additional signals appear in gap regions between these modes. We next expanded the spectral region of the fundamental component (= f_{rep} = 43.0176 MHz) with different spectral range and RBW/VBW, as shown in Figs. 4(b), 4(c), and 4(d). Only single sharp spike was confirmed. We next expanded the spectral region of the 49-th harmonic component (= $49f_{rep}$ = 2107.862 MHz), as shown in Figs. 4(e), 4(f), and 4(g). Again, only the single sharp spike was confirmed. In this way, the intracavity MMI fiber sensor did not generate any parasitic side modes in the RF region.

It is also interesting to investigate the existence of such the parasitic side modes in the optical frequency region. To this end, we prepared a narrow-linewidth CW laser (PLANEX, Redfern

Integrated Optics, Inc., center wavelength: 1,550 nm; FWHM: <2.0 kHz) and phase-locked it to a commercialized OFC (OCLS-HSC-D100-TKSM, Neoark Co., center wavelength = 1560 nm, spectral bandwidth = 20 nm, repetition frequency = 100 MHz, carrier-envelope-offset frequency = 10.5 MHz, phase-locked to the RF frequency standard). Linewidth of the phase-locked CW laser light is estimated to several kHz. Then, the phase-locked CW laser light was interfered with the output light of the MMI-OFC by a fiber coupler (not shown in Fig. 2). Figure 5 shows the RF spectrum of the optical beat signal between the CW laser light and the MMI-OFC light. In addition to the f_{rep} signal, the beat signal (freq. = f_{beat}) between the CW laser light and the most adjacent MMI-OFC mode and its mirror signal (freq. = f_{rep} - f_{beat}) were clearly confirmed. Due to no active stabilization of the repetition frequency and the carrier-envelope-offset frequency in the MMI-OFC, the f_{beat} signal fluctuated with the somewhat broader linewidth; however, no parasitic side modes appear in the optical frequency region.

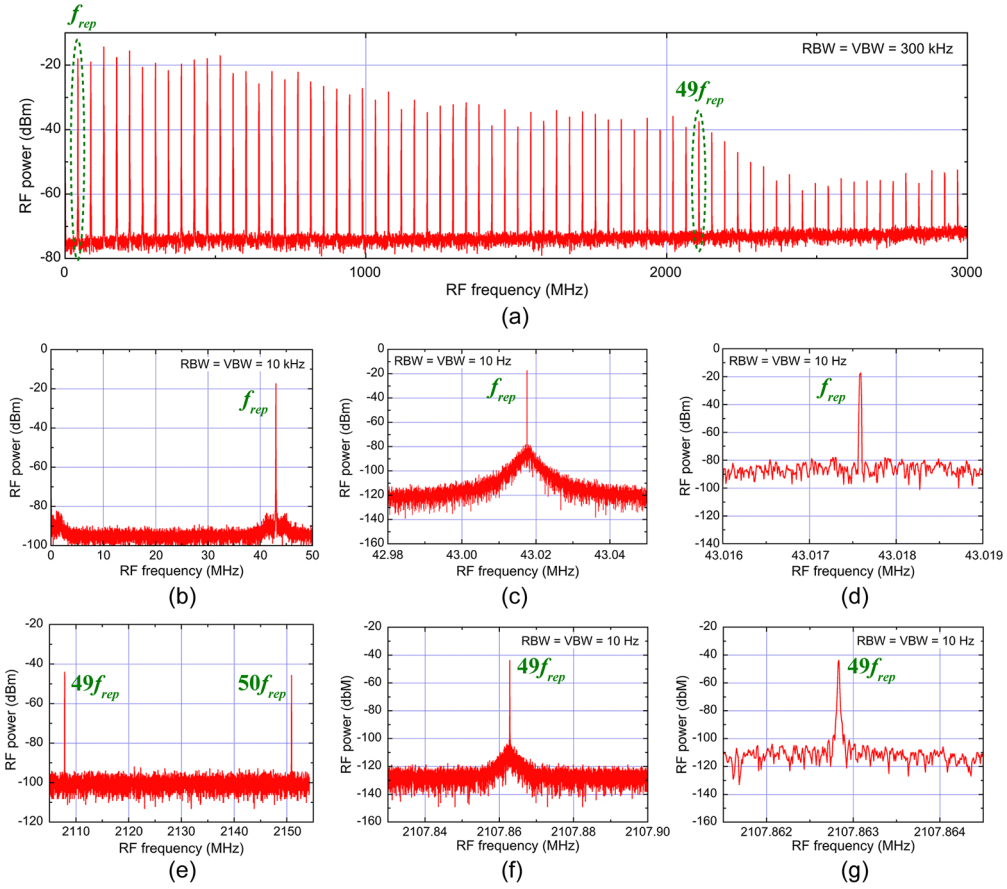

Fig. 4. (a) RF spectrum of the RF comb mode within the frequency range of 3000 MHz RF spectrum of the fundamental component with the frequency range of (b) 50 MHz, (c) 0.07 MHz, and (d) 0.003 MHz. RF spectrum of the 49-th harmonic component with the frequency range of (b) 50 MHz, (c) 0.07 MHz, and (d) 0.003 MHz RBW, resolution bandwidth; VBW, video bandwidth.

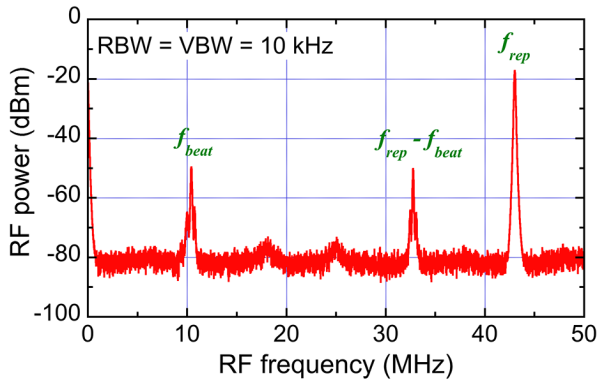

Fig. 5. RF spectrum of the optical beat signal between one mode of the MMI-OFC and a CW laser light phase-locked to another fully stabilized OFC.

We further compare the fluctuation of f_{rep} between the MMI-OFC and the usual OFC. f_{rep} in the MMI-OFC was 43.19 MHz, whereas that in the usual OFC was 43.06 MHz Figure 6 shows

a comparison of the fluctuation in f_{rep} between the usual OFC (blue plots) and the MMI-OFC (red plots) with respect to gate time. The fluctuation in f_{rep} is indicated by the Allan deviation. The fluctuation in f_{rep} showed similar behavior in the usual OFC and the MMI-OFC: the fluctuation decreased at gate times below 0.2 s, whereas it increased at gate times over 0.2 s. The drift behavior of f_{rep} still remained even at gate times greater than 0.2 s, although the temperature of the OFC cavity was stabilized; this behavior is typical in f_{rep}-unstabilized OFCs [42]. The f_{rep} fluctuation in the MMI-OFC reached a minimum value of 0.0302 Hz at a gate time of 0.2 s. Most importantly, the introduction of the MMI fiber sensor into the fiber OFC cavity had little effect on the fluctuation in f_{rep}, enabling us to perform high-precision RI sensing based on the stable f_{rep}.

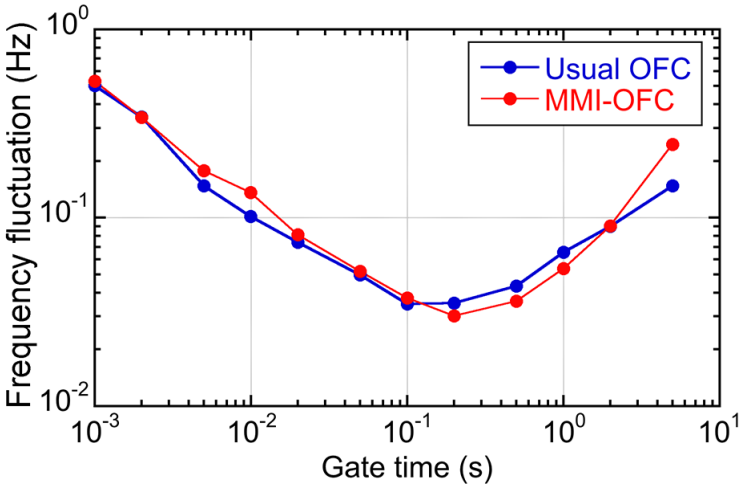

Fig. 6. Comparison of frequency instability between usual OFC and MMI-OFC.

2.2.2 RI-dependent shift of optical spectrum

Next, we investigated the shift of the optical spectrum with respect to the sample RI. Ethanol/water solutions with different mixture ratios (= 0–15 EtOH%, corresponding to 1.333–1.340 RIU) were used as samples with different RIs. We repeated the same experiment for 5 sets of ethanol/water samples with different RIs, and then calculated the mean and the standard deviation of them for each RI. Figure 7(a) shows a comparison of typical optical spectra of the

ethanol/water samples with different RIs. Figure 7(b) shows the magnified spectrum of their peaks in Fig. 7(a). One can confirm the long-wavelength shift of the optical spectrum with increasing RI. Figure 7(c) show the relation between the sample RI and the shift of the center wavelength in the optical spectrum. The corresponding ethanol concentration is shown on the upper horizontal axis in Fig. 7(c). A positive linear relation between them was confirmed with a slope coefficient of 65.7 nm/RIU, indicated by a blue line. For comparison, we conducted a similar experiment using the ethanol/water solution sample (= 0–60 EtOH%, corresponding to 1.333–1.364 RIU) by placing the same MMI fiber sensor outside the cavity to use the MMI fiber sensor in the usual way. The resulting slope coefficient was 53.5 nm/RIU as shown in Fig. 7(d) although the experimental data somewhat deviated from the linear relation. Reasonable match of the slope coefficient between them indicates that the MMI fiber sensor can work as an RI sensor even inside the fiber OFC cavity, in the same manner as the extra-cavity MMI fiber sensor.

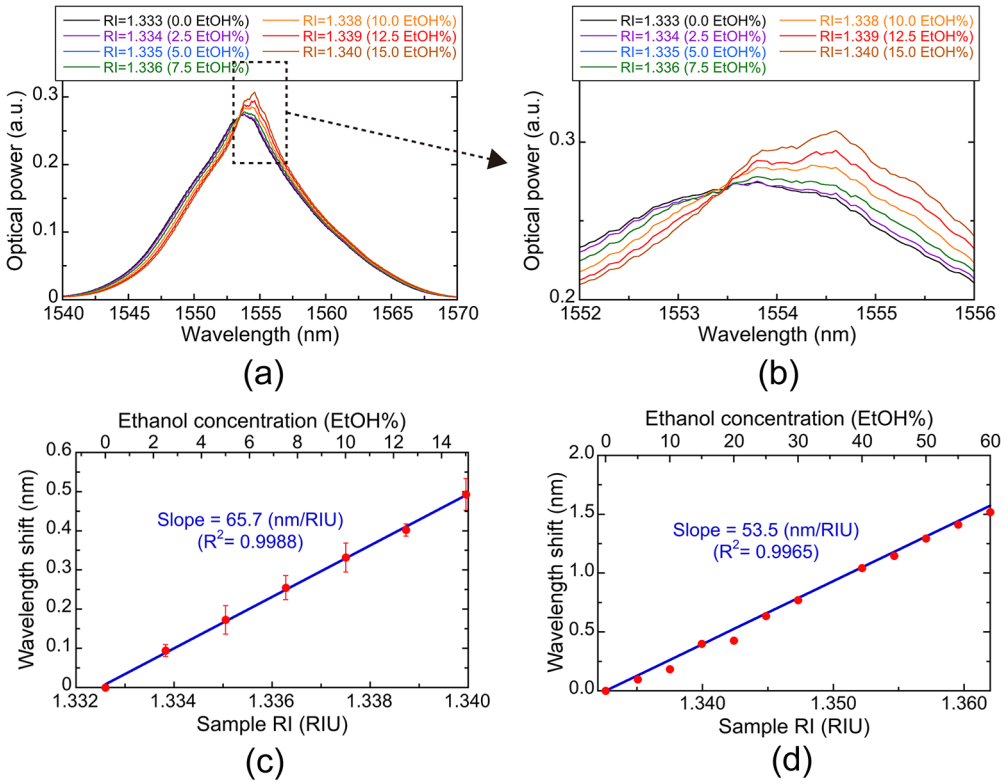

Fig. 7. RI-dependent shift of optical spectrum. (a) Optical spectra of MMI-OFC with respect to different sample RIs and (b) magnified spectra of their peaks. Increasing sample RI causes a long-wavelength shift of the optical spectrum. (c) Relation between sample RI and wavelength shift $\Delta\lambda$ in the MMI-OFC. Plots and error bars indicate the mean and the standard deviation of $\Delta\lambda$ in 5 repetitive measurements. (d) Relation between sample RI and wavelength shift $\Delta\lambda$ in the extra-cavity MMI fiber sensor. Blue line shows a linear approximation by a curve fitting analysis.

2.2.3 RI sensing based on f_{rep} shift

Finally, we performed RI measurement of ethanol/water samples with different mixture ratios (= 0–15 EtOH%, corresponding to 1.333–1.340 RIU) based on a shift in f_{rep}. Figure 8(a) shows the RI-dependent shift of the RF spectrum for f_{rep}, acquired by an RF spectrum analyzer. The linewidth of the RF spectra was limited by the instrumentation resolution of the RF spectrum analyzer rather than the actual linewidth of the f_{rep} signal. Nevertheless, the amount of spectral shift was significantly larger than the spectral linewidth, compared with the RI-dependent shift of the optical spectrum in Figs. 7(a) and 7(b). Such a high ratio of the spectral shift to the spectral linewidth enables high-resolution RI sensing based on RF measurement. Next, we measured f_{rep} values for 5 sets of ethanol/water samples with different RIs by using an RF

frequency counter, and then calculated the mean and the standard deviation of their frequency shift for each RI. Figure 8(b) shows the relation between the sample RI and the f_{rep} shift in the MMI-OFC, indicating a negative linear relation between them with a slope coefficient of -6.19×10^3 Hz/RIU. Considering the positive relation in Fig. 7(c) and the negative net dispersion of the cavity fiber in this wavelength band, this negative slope is valid. Since the f_{rep} fluctuation was 0.0302 Hz at a gate time of 0.2 s [see red plots in Fig. 6], the RI resolution was estimated to be 4.88×10^{-6} RIU. On the other hand, the RI accuracy was estimated to be 5.35×10^{-5} RIU when it was defined as the root mean square (RMS) between the experimental data and the linear approximation. The differences of the RI resolution and accuracy are mainly due to the influence of the cavity and/or sample temperature, as discussed later.

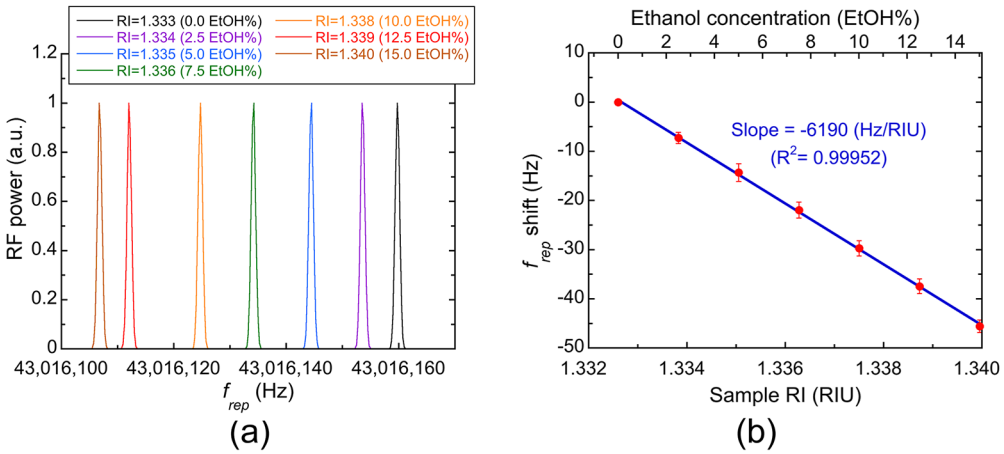

Fig. 8. RI-dependent f_{rep} shift. (a) RF spectra of f_{rep} signal with respect to different sample RI. Increasing sample RI causes decrease of f_{rep}. (b) Relation between sample RI and f_{rep} shift. Plots and error bars indicate the mean and the standard deviation of f_{rep} in 5 repetitive measurements. Blue line shows a linear approximation by a curve fitting analysis.

2.3 Discussion

We first discuss the validity of the RI-dependent f_{rep} shift [Fig. 8(b)]. An RI-dependent optical spectrum shift is converted into an RI-dependent f_{rep} shift via the wavelength dispersion of the cavity fiber [see Fig. 1(b)]. The present MMI-OFC cavity includes a 2.9-meter SMF with anomalous dispersion (= 17 ps/km/nm) and a 1.6-meter EDF with normal dispersion (= -15

ps/km/nm), leading to a net dispersion of 0.0253 ps/nm. From this net dispersion and the slope coefficient of 65.7 nm/RIU in Fig. 7(c), the relation between the time delay and sample RI is given as 1.66 ps/RIU, corresponding to -3.1×10^3 Hz/RIU. This estimated slope is in reasonable agreement with the experimental plots for the MMI-OFC [= -6.19×10^3 Hz/RIU, see Fig. 8(b)]. There are two reasons for the difference between the experimental slope and the estimated one: one is the change in the optical cavity length caused by the Goos-Hänchen shift in the intracavity MMI fiber sensor; the other is the wavelength dispersion of the intracavity MMI fiber sensor. Even including such an influence, the MMI-OFC functions as a correct photonic RF converter for RI.

Next, we discuss the influence of temperature fluctuation in the MMI-OFC cavity because such temperature fluctuation results in thermal expansion or shrinkage of the optical cavity length and hence leads to a change in nL and f_{rep}. We measured f_{rep} shift in the MMI-OFC with a pure water sample (= 0 EtOH%, RI = 1.333 RIU) when the cavity temperature T_{cav} was changed within the range of 20.0 to 21.4ºC. Figure 9(a) shows the relation between the cavity temperature and f_{rep} shift. A linear relation was confirmed between them, and its slope was determined to be -177 Hz/ºC by a linear approximation. On the other hand, the f_{rep} fluctuation in Fig. 6 was 0.0302 Hz at a gate time of 0.2 s. Therefore, if the f_{rep} fluctuation is mainly due to the fluctuation of T_{cav}, T_{cav} is estimated to be stabilized within 1.7×10^{-4} ºC during a time period of 0.2 s.

We also investigated the relation between the sample temperature T_{sam} and the f_{rep} shift because the sample RI depends on both EtOH% and temperature. To this end, we measured f_{rep} shift when changing T_{sam} of a pure water sample (= 0 EtOH%, RI = 1.333 RIU) within the range of 22.0ºC to 25.0ºC, as shown in Fig. 9(b). A linear dependence of f_{rep} shift on T_{sam} was confirmed again; however, the slope constant (= -30.9 Hz/ºC) was 6-times smaller than that of T_{cav}. Therefore, T_{cav} control is more important than T_{sam} control for high-resolution RI sensing.

If the f_{rep} fluctuation is influenced by the fluctuation of T_{sam} rather than that of T_{cav}, T_{sam} is estimated to be stabilized within 9.7×10^{-4} ºC during a time period of 0.2 s. T_{sam} may further influence the RI accuracy because the reproducibility of T_{sam} in repetitive measurements appears in the RI accuracy. From the RI accuracy of 5.35×10^{-5} RIU in Fig. 8(b), the reproducibility of T_{sam} is estimated to be within 0.01ºC. This value is reasonable considering the performance of the temperature controller.

Finally, we have a more in-depth discussion of the proposed method. The benefit of the proposed method was the precise photonic-to-RF conversion of the OFC, which is highlighted by comparing Figs. 7(a) and 8(a). Combination of this function with high-precision RF measurement benefits the high-resolution RI sensing. The achieved RI resolution (= 4.88×10^{-6} RIU) is 10-times higher than that of the previous research [32]. On the other hand, the measurable range of the sample RI was remained within the range of 1.3326 ~ 1.3424 RIU, corresponding to 0 ~ 20 EtOH%, because of the difficulty of maintaining the nonlinear-polarization-rotation-based mode-locking oscillation in MMI-OFC. Also, such nonlinear-polarization-rotation-based mode-locking oscillation limits high reproducibility of f_{rep} due to several degrees of freedom in the MMI-OFC cavity, such as the intracavity polarization controller or the pump LD current. Use of the saturable-absorption-based mode-locking oscillation, in place of the nonlinear-polarization-rotation-based mode-locking oscillation, will overcome these limitations due to its easier mode-locking oscillation and less degrees of freedom in the cavity.

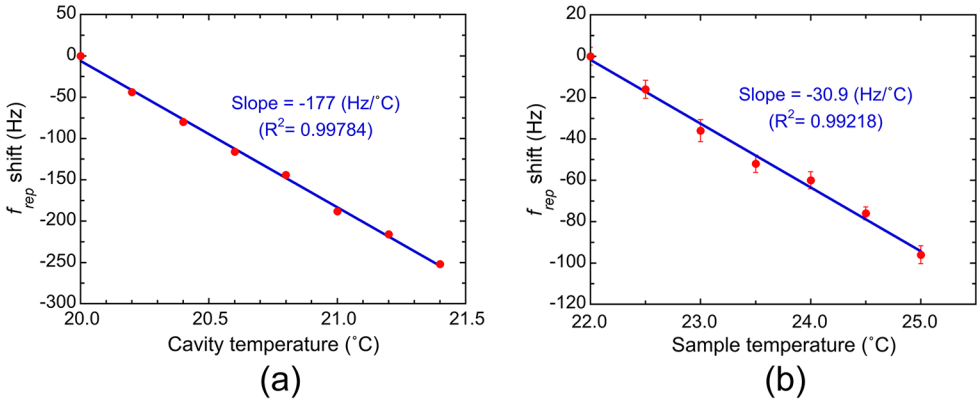

Fig. 9. Dependence of f_{rep} shift on temperature. (a) Cavity temperature dependence and (b) sample temperature dependence. Plots and error bars indicate the mean and the standard deviation of f_{rep} in 5 repetitive measurements. Blue line shows a linear approximation by a curve fitting analysis.

3. Improvement of dynamic range and repeatability in a refractive-index-sensing optical comb by combining saturable-absorber-mirror mode-locking with an intracavity multimode interference fiber sensor

3.1 Principle of operation

Figure 10 shows the principle of operation for a MMI-OFC [34]. The MMI-OFC has a ring-type fiber cavity containing a mode-locker and a MMI fiber sensor. The intracavity of the MMI fiber sensor functions as an RI-dependent tunable optical bandpass filter (bandpass center wavelength = λ_{MMI}) via the multimode interference and the Goos-Hänchen shift on the surface of the MMI fiber sensor. In other words, the intracavity MMI fiber sensor shifts the optical spectrum (λ_{MMI}) of the MMI-OFC depending on the sample RI. The wavelength-shifted MMI-OFC spectrum experiences the wavelength dispersion of the cavity fiber, resulting in the conversion from the RI-dependent optical spectral shift to an RI-dependent shift in the optical cavity length nL. Since f_{rep} of OFC is given by c/nL, where c is the velocity of light in vacuum, a change in the RI of a sample can be read out as an RI-dependent f_{rep} shift (Δf_{rep}).

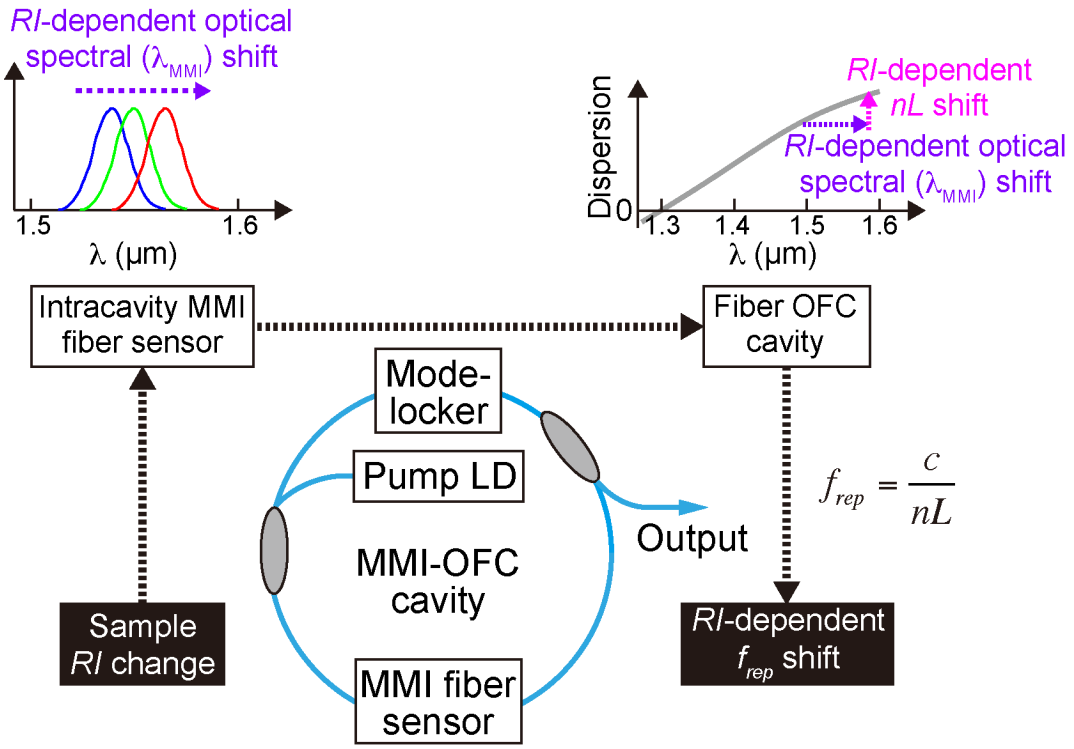

Fig. 10. Principle of operation for MMI-OFC.

3.2 Experimental setup

We modified a mode-locked Er:fiber laser oscillator for the SAM-MMI-OFC, as shown in Fig. 11. This oscillator had a ring cavity, including a 3.3 m length of single-mode fiber (SMF, SMF-28, Corning, dispersion at 1550 nm = 17 ps/km/nm), a 0.5 m length of erbium-doped fiber (EDF, ER80-4/125, LIEKKI, dispersion at 1550 nm = -65 ps/km/nm), a fiber-coupled saturable absorbed mirror (FC-SAM, SAM-1550-4-4ps-FC, BATOP, high reflection band = 1480~1580 nm, absorbance = 4 %, modulation depth = 2.4 %, relaxation time constant ~ 4 ps, mounted on a 1 m SMF cable with FC connector), a polarization-insensitive isolator (ISO, PSSI-55-P-I-N-B-I, AFR), a 70:30 fiber coupler (FC, SBC-1-55-30-1-B-1, AFR), a wavelength-division-multiplexing coupler (WDM, WDM-1-9855-1-L-1-F, AFR), a pumping laser diode (pump LD, BL976-PAG900, Thorlabs, wavelength = 980 nm, power = 900 mW), a fiber circulator (FCIR-55-1-B-1-1, AFR), and an intracavity MMI fiber sensor. The intracavity MMI fiber sensor was composed of a clad-less MMF (FG125LA, Thorlabs, core diameter = 125 μm, fiber length =

58 mm) with a pair of SMFs at both ends (core diameter= 6 μm, clad diameter = 125 μm, fiber length = 54 mm), the detail of which is given elsewhere.[15] Here, we set m to 4 for the use of the intracavity MMI fiber sensor as the RI-dependent tunable bandpass filter. The SAM functions as a stable mode-locker via a fiber circulator. The fiber cavity was enclosed in an aluminum box, and its temperature was controlled to 26.0 °C by a combination of a Peltier heater (TEC1-12708, Kaito Denshi, power = 76 W), a thermistor (PB7-42H-K1, Yamaki) and a temperature controller (TED200, Thorlabs, PID control) [not shown in Fig. 11]. The output light from the oscillator was detected by a photodetector (PD), and f_{rep} was measured by an RF frequency counter (53230A, Keysight Technologies, frequency resolution = 12 digit/s) and an RF spectrum analyzer (E4402B, Keysight Technologies, frequency resolution = 1 Hz), both of which were synchronized to a rubidium frequency standard (FS725, Stanford Research Systems, accuracy = 5×10^{-11} and instability = 2×10^{-11} at 1 s). Additionally, its optical spectrum was measured by an optical spectrum analyzer (AQ6315A, Yokogawa Electric Corp., wavelength accuracy = 0.02 nm, wavelength resolution = 0.02 nm). For comparison, we prepared the NPR-MMI-OFC[15] and enclosed it in the same temperature-controlled box. The specification of the NPR-MMI-OFC was set to be similar to the SAM-MMI-OFC, as shown later. The same MMI fiber sensor was used in the NPR-MMI-OFC.

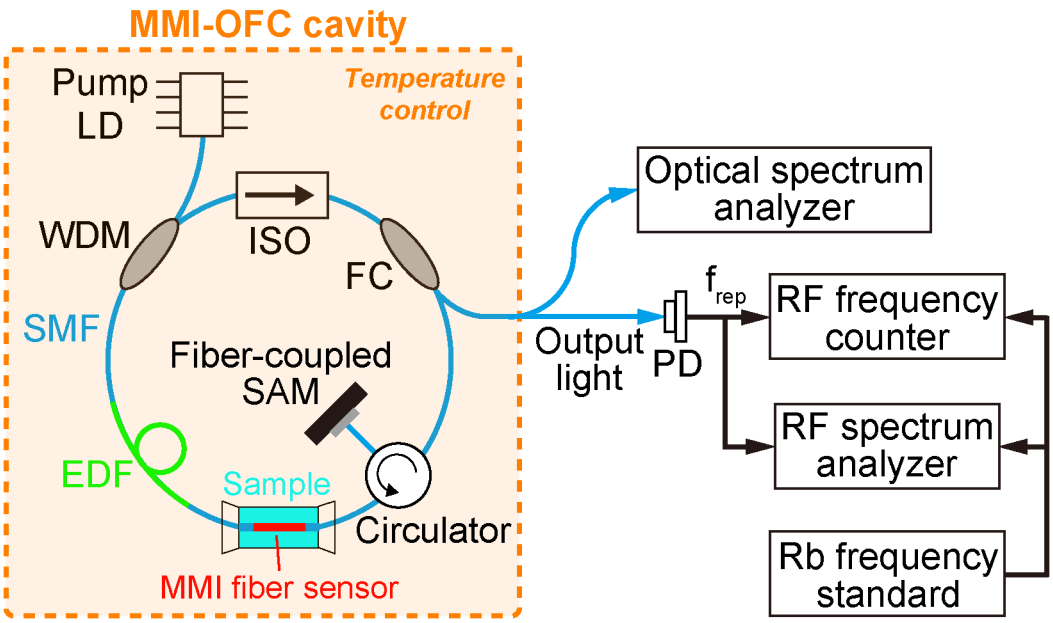

Fig. 11. Experimental setup.

3.3 Results

3.3.1 Basic characteristics of OFC without intracavity MMI fiber sensor

Before evaluating the performance of RI sensing, we compared an optical spectrum and an RF spectrum between the SAM-MMI-OFC and NPR-MMI-OFC. Pure water was used here as a liquid sample. The red and blue plots in Fig. 12(a) show an optical spectrum of the SAM-MMI-OFC (center wavelength = 1558.8 nm, spectral bandwidth = 0.8 nm, mean power = 1.43 mW) and the NPR-MMI-OFC (center wavelength = 1552.2 nm, spectral bandwidth = 7.7 nm, mean power = 1.46 mW), respectively. The soliton mode-locking oscillation was achieved near the zero-dispersion region of the cavity (-0.0338 ps^2 for the SAM-MMI-OFC and -0.0339 ps^2 for the NPR-MMI-OFC). The spectral bandwidth in the SAM-MMI-OFC was significantly narrower than that in the NPR-MMI-OFC. While the SAM-MMI-OFC can be easily mode-locked by the narrower spectral light and, hence, by the longer pulse light, the mode-locking oscillation of the NPR-MMI-OFC needs the broader spectral light and the shorter pulse light together with precise polarization control. Such ease of mode-locking oscillation in the SAM-

MMI-OFC will contribute to the robustness against the cavity disturbance caused by the intracavity MMI fiber sensor. Figure 12(b) compares the RF spectrum of f_{rep} between the SAM-MMI-OFC (red plot) and the NPR-MMI-OFC (blue plot). f_{rep} was 54.86 MHz for the SAM-MMI-OFC and 54.79 MHz for the NPR-MMI-OFC, which are approximately equal. Both RF spectra have a similar linewidth of approximately 1 Hz, which is limited by the instrumentational resolution of the RF spectrum analyzer rather than the actual RF spectrum of f_{rep}. We also compare the frequency instability of f_{rep} between the SAM-MMI-OFC and the NPR-MMI-OFC. The red and blue plots in Fig. 12(c) show the frequency instabilities of f_{rep} with respect to the gate time, which is defined as the ratio of the f_{rep} fluctuation to the mean f_{rep} value. Little difference was observed between them; in other words, the use of SAM in MMI-OFC does not degrade the f_{rep} instability and has the potential to achieve the same RI resolution as the NPR-MMI-OFC.

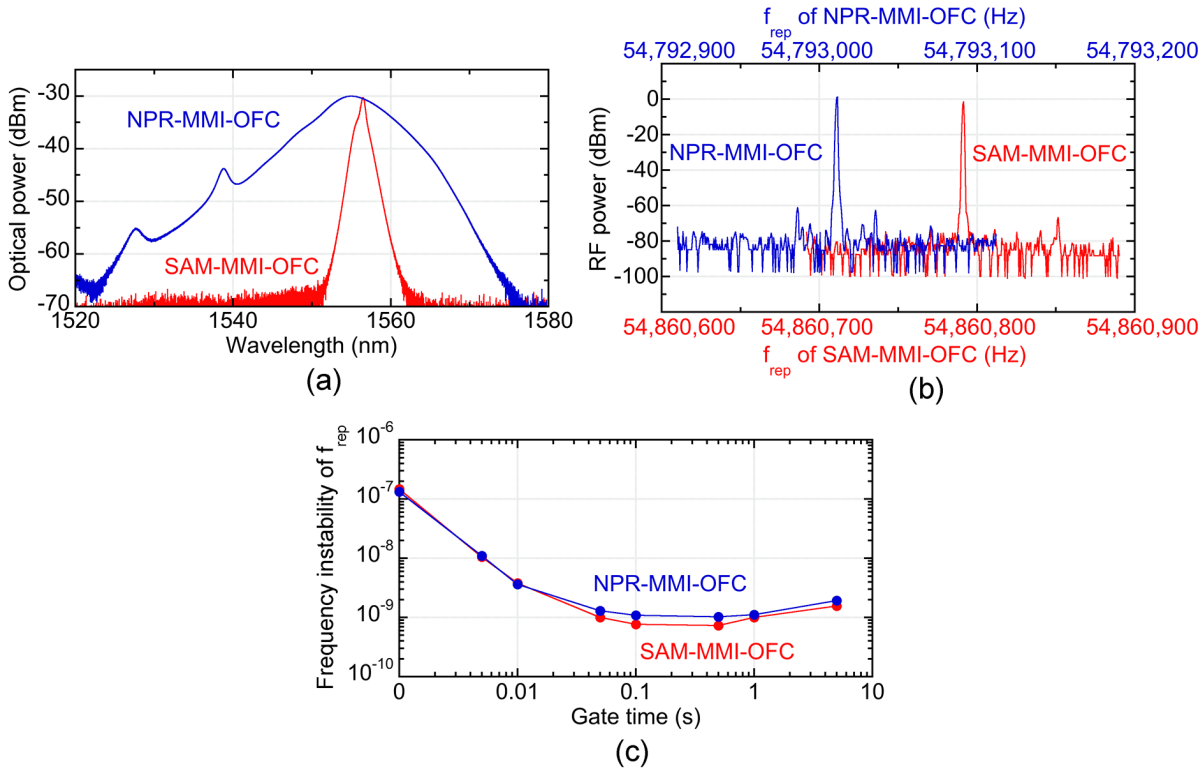

Fig. 12. Comparison of (a) optical spectrum, (b) RF spectrum of frep, and (c) frequency instability of frep between SAM-MMI-OFC and NPR-MMI-OFC.

3.3.2 RI-dependent shift of λ_{MMI} and Δf_{rep}

To confirm the RI sensing capability in the optical region, we first investigated the RI-dependent λ_{MMI} shift in the SAM-MMI-OFC and the NPR-MMI-OFC. Mixtures of ethanol and pure water were used here as liquid samples. The sample RI was adjusted by changing the ethanol and water mixture ratio. Furthermore, the temperature of the sample was controlled at 22 °C by a combination of a K-type thermocouple (TJA-550K, AS ONE), a cord heater (603-60-69-01, Tokyo Glass Kikai, power = 15 W), and a temperature controller (TJA-550, AS ONE, PID control, display resolution = 0.1 °C). The relationship between the ethanol volume concentration EC (unit: EtOH%) and the sample RI (unit: RIU) is given by RI = $1.3326+4.90\times10^{-4}\times$EC [41]. The resulting RI-dependent λ_{MMI} shift was determined to be 94.5 nm/RIU for the SAM-MMI-OFC and 67.8 nm/RIU for NPR-MMI-OFC, respectively (not shown). We next evaluated the relation between the sample RI and the f_{rep} shift (Δf_{rep}) in the SAM-MMI-OFC and NPR-MMI-OFC. Figures 13(a) and 13(b) respectively show the RI-dependent RF spectrum shift of f_{rep} obtained by the SAM-MMI-OFC and the NPR-MMI-OFC for the ethanol/water samples with different mixture ratios (= 0–20 EtOH%, corresponding to 1.333–1.342 RIU) and acquired by an RF spectrum analyzer. The magnitude of the spectral shift was significantly larger than that of the spectral linewidth in both. Then, we measured the RI-dependent Δf_{rep} more precisely by using an RF frequency counter, as shown in Fig. 13(c). Although the linear relation was confirmed in the SAM-MMI-OFC and the NPR-MMI-OFC, the former shows better linearity than the latter. The RF slope coefficient was determined to be -5.82 Hz/EtOH% for the SAM-MMI-OFC and -4.01 Hz/EtOH% for the NPR-MMI-OFC. The RF slope coefficient ratio [= (-5.82 Hz/EtOH%)/(-4.01 Hz/EtOH%) = 1.45] significantly agrees with the optical slope coefficient ratio of the SAM-MMI-OFC to the NPR-MMI-OFC [= (94.5 nm/RIU)/(67.8 nm/RIU) = 1.39]; the difference in the RF slope coefficient between the SAM-MMI-OFC and the NPR-MMI-OFC is mainly due to the difference in the optical slope

coefficient between the two. From these slope coefficients and the frequency fluctuation of f_{rep}, the RI resolution was determined to be 3.37×10^{-6} for the SAM-MMI-OFC and 6.92×10^{-6} for the NPR-MMI-OFC at a measurement time of 0.5 s.

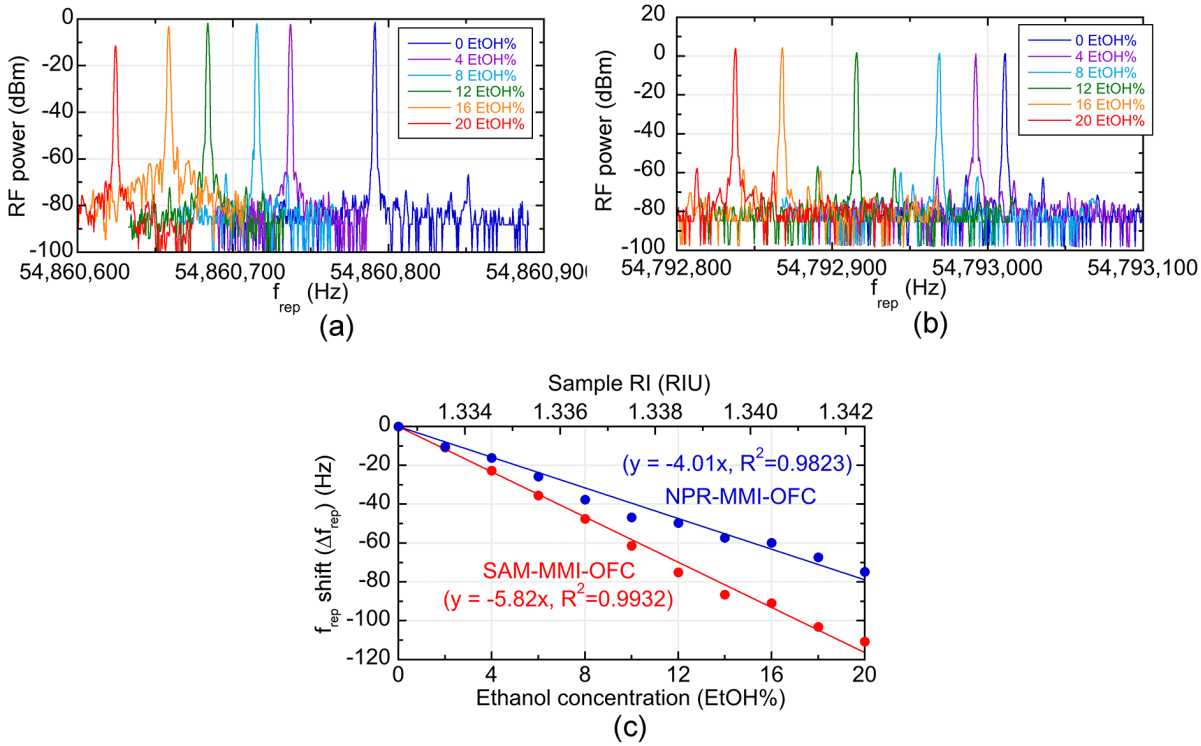

Fig. 13. RI-dependent f_{rep} shift in (a) SAM-MMI-OFC and (b) NPR-MMI-OFC. (c) Relation between ethanol concentration or sample RI and f_{rep} shift (Δf_{rep}) in SAM-MMI-OFC (red plot) and NPR-MMI-OFC (blue plot).

We further investigated the RI-dependent Δf_{rep} of water/ethanol samples within a wider range of mixture ratio (0−100 EtOH%, corresponding to 1.333–1.382 RIU). Figure 14(a) shows the RI-dependent Δf_{rep} of the water/ethanol sample in the SAM-MMI-OFC. The SAM-based mode-locking oscillation was maintained in all ethanol concentrations. The resulting slope coefficient at the lower concentrations was larger than that at the higher concentrations because the RI value of the water/ethanol mixture increased from the low concentration (= 0−80 EtOH%), reached a plateau approximately 80 %, and decreased in the higher concentrations (= 80−100 EtOH %) [33]. Figure 14(b) shows the RI-dependent Δf_{rep} of the water/ethanol sample in the NPR-MMI-OFC. In contrast to the SAM-MMI-OFC, the NPR-based mode-locking oscillation

was lost four times due to the lower robustness against the cavity disturbance caused by the intracavity MMI fiber sensor. When we activated the mode-locking oscillation again by fine adjustment of an intracavity polarization controller, the f_{rep} value significantly jumped from the f_{rep} value before the mode-locking oscillation was lost. As a result, the RI-dependent Δf_{rep} slope shows several discontinuity points. Such discontinuity points hamper the wide dynamic range of RI sensing in the NPR-MMI-OFC. The dynamic range of RI sensing in the SAM-MMI-OFC and the NPR-MMI-OFC is given by

$$DR_{SAM} = 10\log\frac{RI_{max} - RI_{min}}{RI\ resolution} = 10\log\frac{1.3792 - 1.3326}{3.37\times10^{-6}} = 41.4\ dB, \tag{5}$$

$$DR_{NPR} = 10\log\frac{1.3792 - 1.3326}{6.92\times10^{-6}} = 33.3\ dB, \tag{6}$$

where RI_{max} and RI_{min} are the maximum and minimum RI values. This comparison clearly indicates the superiority of the SAM-MMI-OFC over the NPR-MMI-OFC for a wide dynamic range of RI sensing. The maximum RI will be limited by the RI of the clad-less MMF (= 1.444 RIU) because the MMI fiber sensor is based on the total reflection at a boundary between the clad-less MMF surface and the sample.

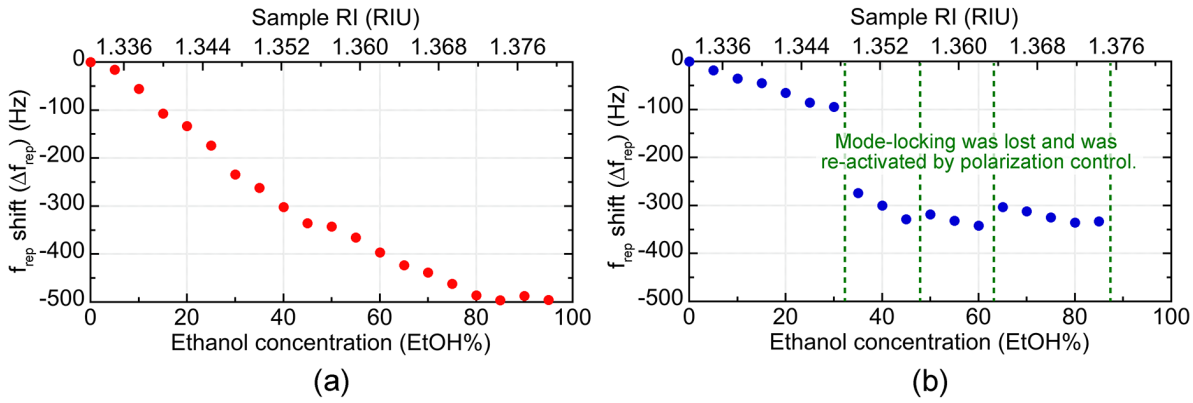

Fig. 14. Relation between ethanol concentration or sample RI and f_{rep} shift (Δf_{rep}) in (a) SAM-MMI-OFC and (b) NPR-MMI-OFC.

We evaluated the repeatability of f_{rep} in the SAM-MMI-OFC and the NPR-MMI-OFC.

Figure 15(a) shows the temporal change of f_{rep} in the SAM-MMI-OFC when the mode-locking oscillation was disrupted by turning the pumping LD off. Due to the self-starting of the mode-locking oscillation without the need for additional adjustment of the intracavity component, the f_{rep} values were recovered with high repeatability before and after the disruption. The slow temporal change of f_{rep} was mainly due to the residual thermal drift of nL. However, the temporal behavior of f_{rep} was almost continuous even though the mode-locking oscillation was disrupted. Frequency deviation before and after disruption of the mode-locking oscillation was 0.60±0.66 Hz for 4 disruptions, corresponding to a repeatability of $(1.10\pm1.21)\times10^{-8}$ in f_{rep}. This repeatability of f_{rep} is equivalent to the repeatability of the RI measurement. On the other hand, with the NPR-MMI-OFC, it is difficult to activate the mode-locking oscillation as self-starting when the mode-locking oscillation is disrupted by turning the pumping LD off. The NPR-MMI-OFC needs the precise adjustment of the polarization controller for the activation of the mode-locking oscillation. As a result, f_{rep} increased by several tens of Hz at every disruption point, even though the scale of the polarization controller was set to that before the disruption, as shown in Fig. 15(b). Frequency deviation before and after disruption of the mode-locking oscillation was 46.0±4.67 Hz for 3 disruptions, corresponding to the f_{rep} repeatability of $(8.40\pm0.85)\times10^{-7}$. Thus, the SAM-MMI-OFC has better f_{rep} repeatability of than the NPR-MMI-OFC.

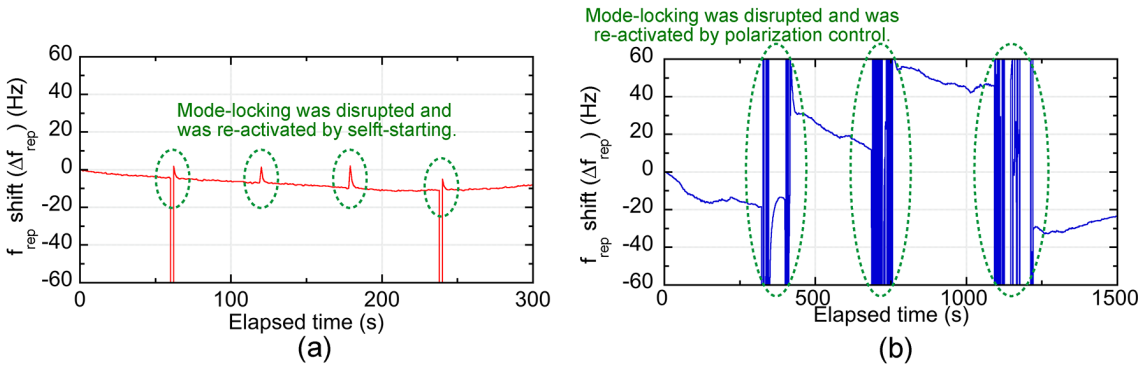

Fig. 15. Temporal change in f_{rep} when the mode-locking oscillation was disrupted. (a) SAM-MMI-OFC and (b) NPR-MMI-OFC.

3.4. Discussion

We here discuss a possibility of the absolute measurement of the sample RI based on one-to-one correspondence between sample RI and f_{rep}. In the previous research of MMI-OFC [34], the low repeatability of f_{rep} in the NPR-MMI-OFC [see Fig. 15(b)] hampers such absolute RI measurement. Therefore, the relative measurement was performed based on one-to-one correspondence between the sample RI and f_{rep} shift (Δf_{rep}). Use of SAM in MMI-OFC benefits from high repeatability of f_{rep} [see Fig. 15(a)] in addition to wide dynamic range of RI sensing. However, the slow temporal change of f_{rep} was still remained due to the residual thermal drift of nL even though the temperature control of fiber cavity was activated. This remained change will be the last barrier preventing the absolute measurement of the sample RI. One possible method to get rid of this barrier is to compensate the drifted f_{rep} by another measured parameter (for example, carrier-envelope-offset frequency of OFC, optical power, optical spectrum, and so on) related with thermal condition of the fiber cavity. Work is in progress to achieve the absolute measurement of the sample RI based on one-to-one correspondence between sample RI and f_{rep}.

4. Refractive index sensing with temperature compensation by a multimode-interference fiber-based optical frequency comb sensing cavity

4.1 Experimental setup

Figure 16 shows the configuration of an MMI-OFC sensing cavity. The MMI-OFC sensing cavity is comprised of a fiber OFC ring cavity with an intracavity MMI fiber sensor. The MMI fiber sensor is composed of a clad-less multi-mode fiber (MMF) with a pair of single-mode fibers (SMFs) at the two ends [8]; it has good compatibility with fiber OFC cavities [34, 35]. The intracavity MMI fiber sensor acts as a RI-dependent tunable optical bandpass filter at the multi-mode interference wavelength λ_{MMI}. λ_{MMI} is given by Eq. (3). Thus, the optical spectrum of the OFC shows the RI-dependent shift owing to the intracavity MMI fiber sensor, namely, λ_{MMI} shift ($\Delta\lambda_{MMI}$).

On the other hand, the OFC exhibits the comb-tooth-like ultradiscrete multimode spectrum with a constant frequency spacing f_{rep} given by Eq. (1). Since f_{rep} is determined by the optical cavity length nL, it is sensitive to the cavity disturbance changing nL; in other words, f_{rep} can be used for quantitative analysis of a physical quantity acting as the cavity disturbance. The intracavity MMI fiber sensor will change the optical cavity length at the intracavity MMI fiber sensor and the group RI of the cavity fiber owing to the spectral shift of the OFC, leading to the RI-dependent f_{rep} shift, namely, Δf_{rep}.

λ_{MMI} and f_{rep} are shifted by a temperature change of a sample because the temporal change leads to a change of sample RI and/or changes of RI and geometrical shape in the MMI sensor

fiber. Thus, by observing $\Delta\lambda_{MMI}$ and Δf_{rep}, we consider realizing the simultaneous measurement of the RI and sample temperature as follows,

$$\begin{bmatrix} \Delta f_{rep} \\ \Delta\lambda_{MMI} \end{bmatrix} = \begin{bmatrix} \frac{\partial f_{rep}}{\partial C} & \frac{\partial f_{rep}}{\partial T} \\ \frac{\partial \lambda_{MMI}}{\partial C} & \frac{\partial \lambda_{MMI}}{\partial T} \end{bmatrix} \begin{bmatrix} \Delta C \\ \Delta T \end{bmatrix}, \tag{7}$$

where ΔC and ΔT are RI-related sample parameters, *i.e.*, sample concentration and temperature, respectively. The coefficient matrix is comprised of the slope coefficients between $\Delta\lambda_{MMI}$ or Δf_{rep} and ΔC or ΔT. From Eq. (7), if the coefficient matrix is regular, one can determine ΔC and ΔT from the simultaneous measurement of $\Delta\lambda_{MMI}$ and Δf_{rep} and the inverse matrix calculation of them.

To demonstrate the MMI-OFC sensing cavity with the temperature compensated RI sensing, a custom-built ring-cavity erbium-doped fiber (EDF) laser with an intracavity MMI fiber sensor, which was mode-locked by a nonlinear polarization rotation technique, was employed as an OFC generator (the fundamental comb spacing or repetition rate, 43 MHz; the center wavelength, 1555 nm; and the spectral bandwidth, 15 nm). The intracavity MMI-fiber sensor was made with a core-less multimode fiber (MMF, the core diameter, 125 μm; the length, 58 mm, FG125LA, Thorlabs) spliced with single-mode fibers (SMF-28-100, Thorlabs) at each terminal. The intracavity MMI-fiber sensor was sunk in a liquid sample with a glass tube. The glass tube had an inlet port and an outlet port to externally change and stir the liquid sample. $\Delta\lambda_{MMI}$ or Δf_{rep} were obtained with an optical spectrum analyzer (OSA, AQ6315A, Yokogawa Electric Corp.), an RF spectrum analyzer (RFSA, E4402B, Keysight Technologies), or an RF frequency counter (53230A, Keysight Technologies).

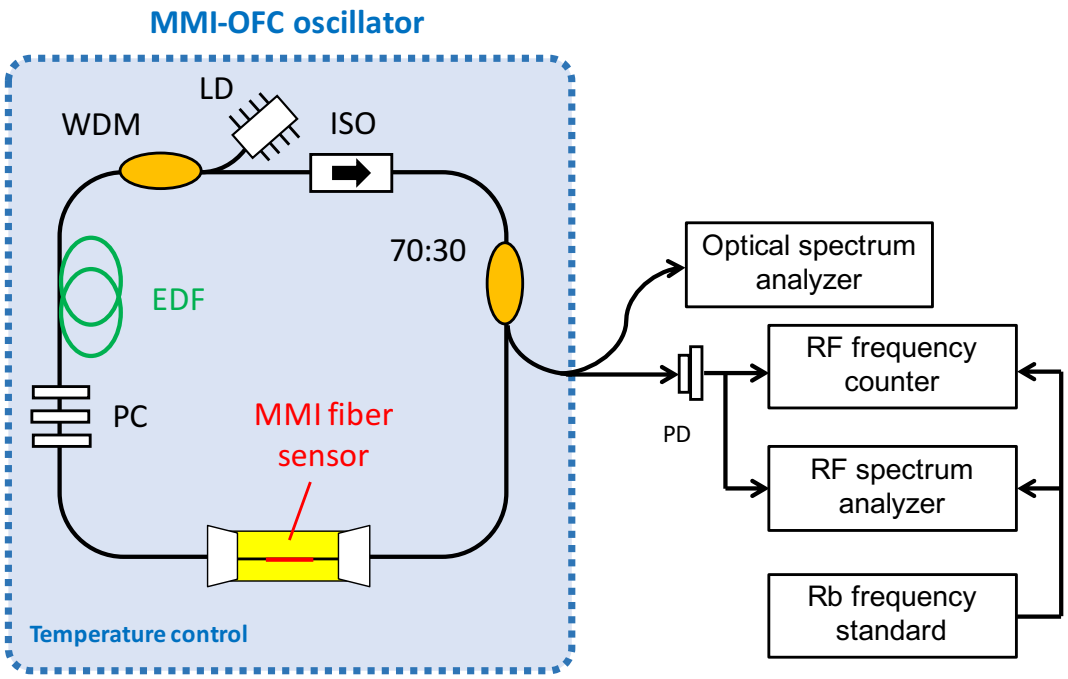

Fig. 16. Schematic diagram of the MMI-OFC. PC, polarization controller for mode-locking; EDF, Er-doped fiber; WDM, wavelength division multiplexer; ISO, polarization independent isolator; 70:30, branch coupler; LD, laser diode; PD, photo detector.

4.2 Results

4.2.1 Temperature dependencies of $\Delta\lambda_{MMI}$ and Δf_{rep} in the MMI-OFC sensing cavity

We first investigated $\Delta\lambda_{MMI}$ and Δf_{rep} with respect to different sample temperatures. The ethanol/water solution (ethanol concentration of 0−15 % v/v with interval of 5 % v/v) was used for samples with different temperatures (26.5−29.0 ºC with interval of 0.5 ºC). The same experiment was repeated for 3 sets of ethanol/water samples with each temperature, and their standard deviations under each of the samples' temperatures were determined.

Figure 17(a) shows the temperature-dependent optical spectra of the MMI-OFC sensing cavity for the ethanol concentration of 0 % v/v. Figure 17(b) shows the relation between sample temperature and $\Delta\lambda_{MMI}$ with respect to different ethanol concentrations. We confirmed the temperature-dependent increase of $\Delta\lambda_{MMI}$. The slope coefficients between temperature and $\Delta\lambda_{MMI}$ were determined to be 0.016 nm/ºC for 0 % v/v, 0.022 nm/ºC for 5 % v/v, 0.021 nm/ºC for 10 % v/v, and 0.018 nm/ºC for 15 % v/v. Thus, the mean slope coefficient, namely, $\partial\lambda_{MMI}/\partial T$,

was obtained to be 0.020 nm/ºC. The accuracy of the temperature-dependent $\Delta\lambda_{MMI}$ was 3.9×10^{-3} nm, which was defined by the root mean square error between the measured plots and its fitting line in Fig. 17(b).

Figure 17(c) shows the temperature-dependent RF spectra of the MMI-OFC sensing cavity for the ethanol concentration of 0 % v/v. Figure 17(d) shows the relation between sample temperature and Δf_{rep} with respect to different ethanol concentrations. We confirmed the temperature-dependent decrease of Δf_{rep}. The slope coefficients between temperature and Δf_{rep} were determined to be -18.01 Hz/ºC for 0 % v/v, -23.63 Hz/ºC for 5 % v/v, -19.74 Hz/ºC for 10 % v/v, and -19.00 Hz/ºC for 15 % v/v, respectively. Thus, the mean slope coefficient, namely, $\partial f_{rep}/\partial T$, was found to be -20.46 Hz/ºC. An opposite sign of slope coefficient between the temperature-dependent $\Delta\lambda_{MMI}$ and Δf_{rep} was obtained. The accuracy of the temperature-dependent Δf_{rep} was 1.17 Hz, which was defined by the root mean square error between the measured plots and its fitting line in Fig. 17(d).

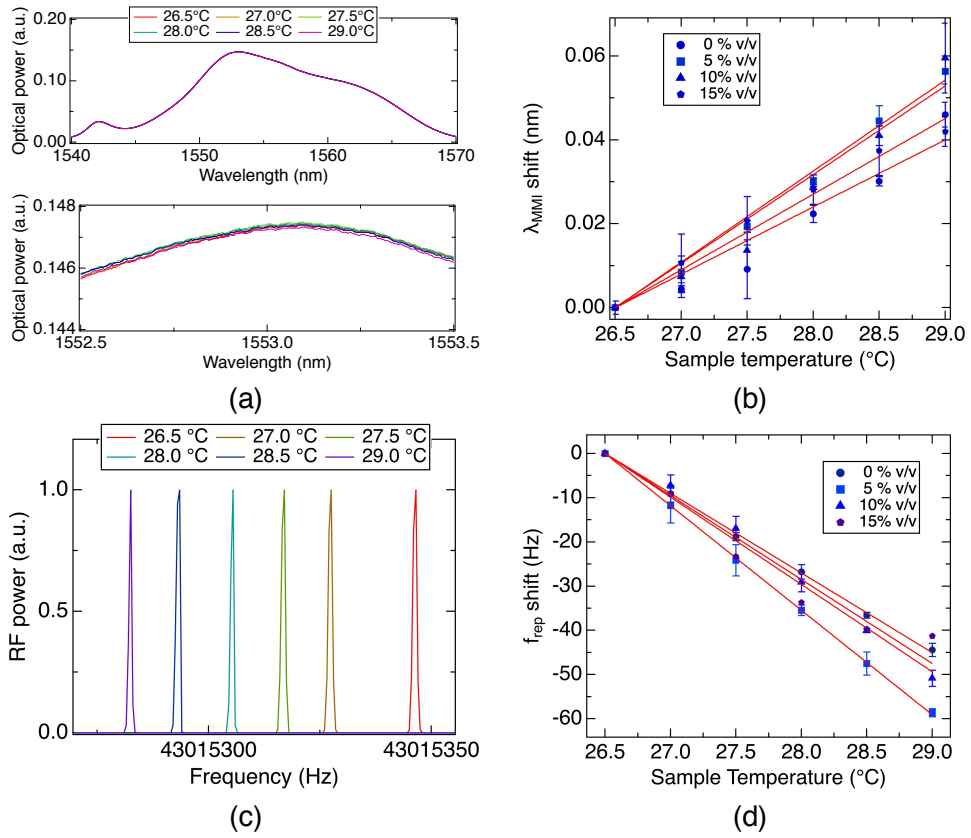

Fig. 17. Temperature-dependent optical spectral shift and RF spectral shift. (a) Optical spectral shift with respect to temperature change. (b) Temperature sensitivity of optical spectrum with respect to different ethanol concentrations. (c) RF spectral shift with respect to temperature change. (d) Temperature sensitivity of RF spectrum with respect to different ethanol concentrations.

4.2.2 RI-related concentration dependencies of $\Delta\lambda_{MMI}$ and Δf_{rep} in the MMI-OFC sensing cavity

We next investigated $\Delta\lambda_{MMI}$ and Δf_{rep} with respect to material-dependent RI for which the different ethanol concentrations of the liquid sample were used. The ethanol/water solution (ethanol concentrations of 0−15 % v/v with interval of 3 % v/v) was used for samples with different temperatures (26.0−29.0 ºC with interval of 1 ºC). The same experiment was repeated for 3 sets of ethanol/water samples with each concentration, and their standard deviations were determined for each of the sample concentrations.

Figure 18(a) shows the concentration-dependent optical spectra of the MMI-OFC sensing cavity at a constant temperature of 26 ºC. Figure 18(b) shows the relation between sample concentration and $\Delta\lambda_{MMI}$ with respect to different sample temperatures. We confirmed the

concentration-dependent increase of $\Delta\lambda_{MMI}$. The slope coefficients between temperature and $\Delta\lambda_{MMI}$ were determined to be 0.029 nm/% v/v for 26.0 ºC, 0.034 nm/% v/v for 27.0 ºC, 0.028 nm/% v/v for 28.0 ºC, and 0.035 nm/% v/v for 29.0 ºC. Thus, the mean slope coefficient, namely, $\partial\lambda_{MMI}/\partial C$, was obtained to be 0.0315 nm/% v/v. The accuracy of the concentration-dependent $\Delta\lambda_{MMI}$ was 8.7×10^{-3} nm, which was defined by the root mean square error between the measured plots and its fitting line in Fig. 18(b).

Figure 18(c) shows the concentration-dependent RF spectra of the MMI-OFC sensing cavity at a constant temperature of 26 ºC. Figure 18(d) shows the relation between sample concentration and Δf_{rep} with respect to different sample temperatures. We confirmed the temperature-dependent decrease of Δf_{rep}. The slope coefficients between temperature and Δf_{rep} were determined to be -3.10 Hz/% v/v for 26.0 ºC, -2.66 Hz/% v/v for 27.0 ºC, -3.05 Hz/% v/v for 28.0 ºC, and -3.03 Hz/% v/v for 29.0 ºC. Thus, the mean slope coefficient, namely, $\partial f_{rep}/\partial C$, was obtained to be -2.96 Hz/% v/v. An opposite sign of the slope coefficient between the temperature-dependent $\Delta\lambda_{MMI}$ and Δf_{rep} was confirmed again. The accuracy of the concentration-dependent Δf_{rep} was 0.85 Hz, which was defined by the root mean square error between the measured plots and its fitting line in Fig. 18(d).

According to the results of the temperature and RI-related concentration dependencies, we can estimate the precision of the MMI-OFC sensing cavity. The precision of the temperature was 0.08ºC, which is estimated from Eq. (7) by applying the accuracies of $\Delta\lambda_{MMI}$ of 3.9×10^{-3} nm and Δf_{rep} of 1.17 Hz obtained by Figs. 17(b) and 17(d). The precision of the RI-related concentration measurements with the MMI-OFC sensing cavity was estimated to be 0.34% v/v corresponding to 1.6×10^{-4} RIU, which is estimted from Eq. (7) by applying the accuracies of $\Delta\lambda_{MMI}$ of 8.7×10^{-3} nm and Δf_{rep} of 0.85 Hz obtained by Figs. 18(b) and 18(d). This result indicates that the MMI-OFC sensing cavity has the potential for RI sensing with temperature compensation with high precision.

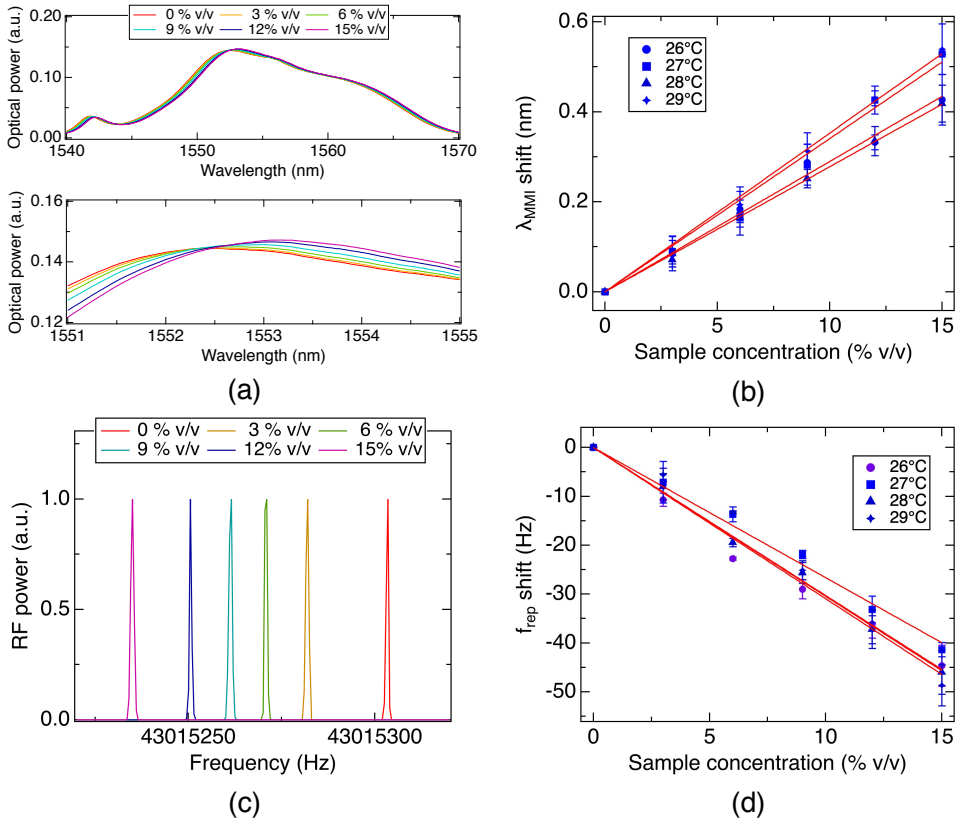

Fig. 18. Concentration-dependent optical spectral shift and RF spectral shift. (a) Optical spectral shift with respect to sample ethanol-concentration change. (b) Ethanol-concentration sensitivity of optical spectrum under constant sample temperature. (c) RF spectral shift with respect to ethanol-concentration change. (d) Ethanol-concentration sensitivity of RF spectrum under constant sample temperature.

4.2.3 Simultaneous measurement of temperature and concentration of a liquid sample

To highlight the proposed method, we demonstrated simultaneous measurement of temperature and RI-related concentration of an ethanol/water solution. We first increase the temperature of a sample stepwise from 26.5 ºC to 29.0 ºC by a heater attached to the liquid sample tube under a constant ethanol concentration of 0 % v/v. We also gently stirred the sample by flowing it in and out using a syringe after changing the temperature to achieve a uniform temperature of the sample. As shown in Figs. 19(a) and 19(b), we clearly confirmed the temperature-dependent $\Delta\lambda_{MMI}$ increase and Δf_{rep} decrease. Then, we determined ΔC and ΔT by substituting the measured $\Delta\lambda_{MMI}$ and Δf_{rep} for Eq. (7) as shown in Figs. 19(c) and 19(d). The determined ΔC and ΔT values well reflect their actual changes: stable concentration within 1 % v/v and step-

by-step increase of temperature by 0.5 ºC within the deviation of below 0.3 ºC from the actual change. If the temperature compensation was not performed, in which the Δn was determined with only Δf_{rep}, the estimation error of ΔC was degraded to 16.9 % v/v by the temperature change from 26.5 ºC to 29.0 ºC, as shown by the green line in Fig. 19(c).

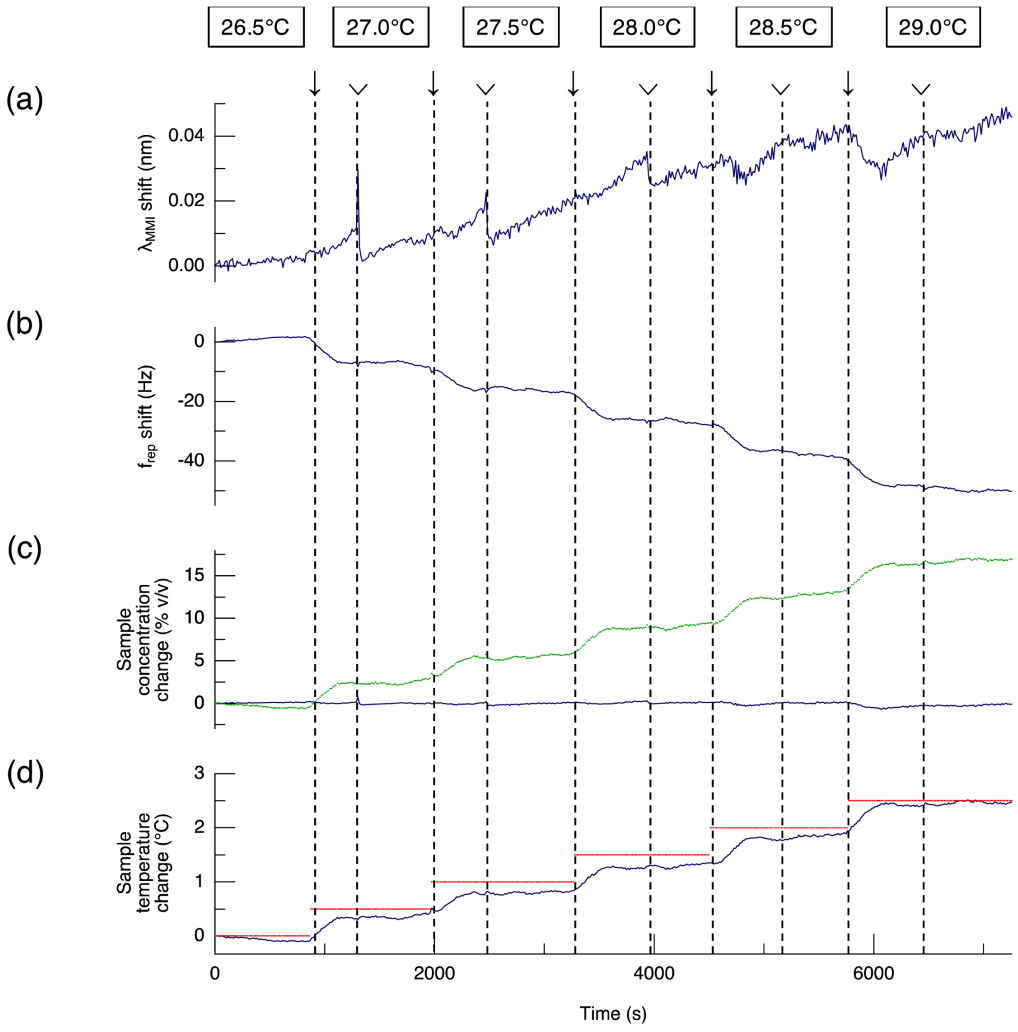

Fig. 19. Simultaneous measurement of temperature and RI-related concentration of an ethanol/water solution under the variable temperature (26.5-29.0ºC) and the constant ethanol concentration (0% v/v). (a) Temporal behavior of the λ_{MMI} shift. (b) Temporal behavior of f_{rep} shift. (c) Temporal behavior of the sample concentration change estimated by using only Δf_{rep} (green line) and by using both the Δf_{rep} and $\Delta\lambda_{MMI}$ via Eq. (7) (blue line). (d) Temporal behavior of the sample concentration change estimated by using both the Δf_{rep} and $\Delta\lambda_{MMI}$ via Eq. (7). The red line in Fig. 19(d) indicates the setting temperature of the ethanol/water solution. The arrows indicate the times at which the temperature was changed. The arrow heads indicate the times at which the sample was stirred.

We next increase the sample concentration stepwise from 0 % v/v to 15 % v/v by adding ethanol with a pipette under a constant temperature (26.0 ºC). We also gently stirred the sample by flowing it in and out using a syringe after the ethanol application to achieve a uniform sample concentration. As shown in Figs. 20(a) and 20(b), we clearly confirmed the concentration-dependent $\Delta\lambda_{MMI}$ increase and Δf_{rep} decrease. Then, we determined ΔC and ΔT by substituting the measured $\Delta\lambda_{MMI}$ and Δf_{rep} for Eq. (7) as shown in Figs. 20(c) and 20(d). The determined ΔC and ΔT values again well reflect their actual changes. The measurement stability was approximately 1 % v/v in the concentration estimation and below 0.2 ºC in the temperature estimation. Importantly, even in the fixed temperature condition, the temperature instability due to the limited control capability of the sample temperature can be compensated by using the proposed method.

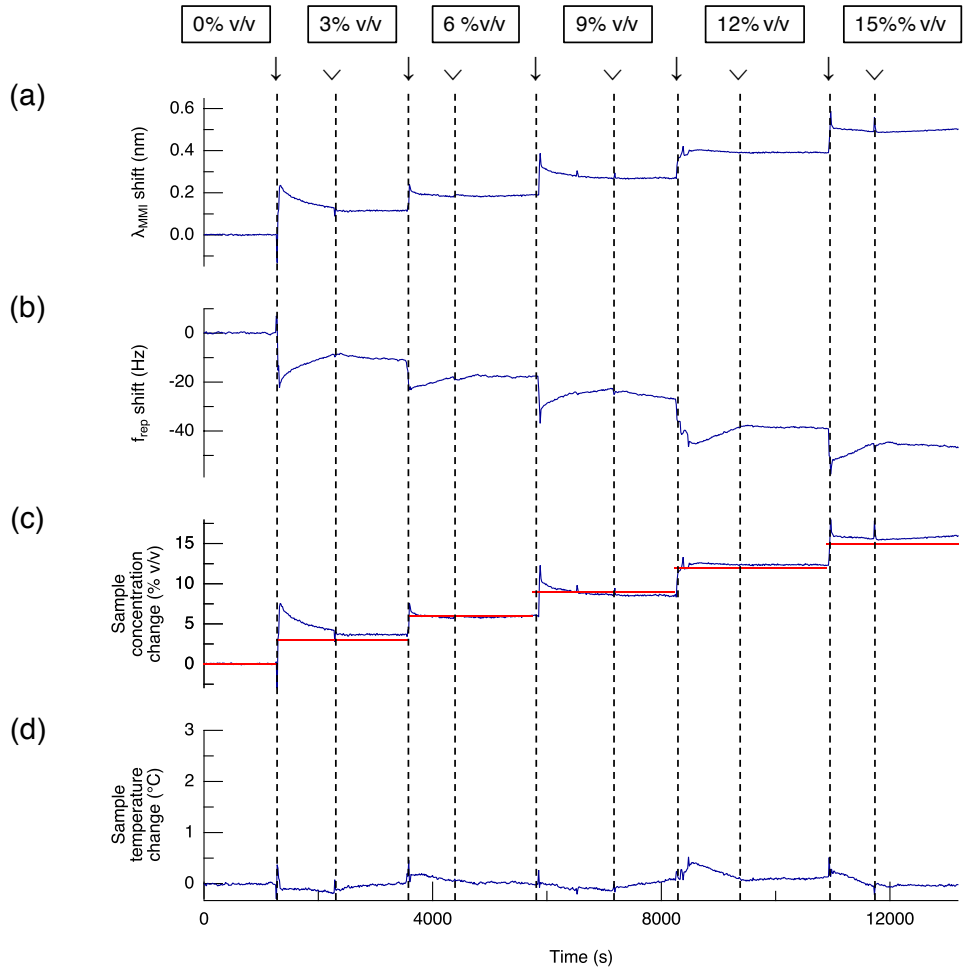

Fig. 20. Simultaneous measurement of temperature and RI-related concentration of an ethanol/water solution under the constant temperature (26.0ºC) and the variable ethanol concentration (0-15% v/v). (a) Temporal behavior of the λ_{MMI} shift. (b) Temporal behavior of f_{rep} shift. (c) Temporal behavior of the estimated sample concentration change. The red line in Fig. 20(c) indicates the actual concentration of the ethanol/water solution. (d) Temporal behavior of the estimated sample concentration change. The arrows indicate the times at which the ethanol was applied. The arrow heads indicate the times at which the sample was stirred.

We finally changed both the concentration and temperature of a sample. The protocol of the experiment is as follows:

(1) The ethanol concentration and temperature were initially set to 0 % v/v and 27.0 ºC, respectively.

(2) The ethanol temperature and concentration were simultaneously increased by 0.5 ºC and 2.5 % v/v, respectively.

(3) The ethanol temperature and concentration were simultaneously increased by 2.5% v/v and decreased by 0.5ºC, respectively.

(4) The ethanol temperature and concentration were simultaneously increased by 1.0 ºC and 2.5 % v/v, respectively.

(5) The ethanol concentration and temperature were simultaneously increased by 2.5 % v/v and decreased by 0.5 ºC, respectively.

These changes were sensitively reflected in $\Delta\lambda_{MMI}$ and Δf_{rep}, as shown in Figs. 21(a) and 21(b), respectively. By using Eq. (7), ΔC and ΔT were determined, as shown in Figs. 21(c) and 21(d). Both ΔC and ΔT could be determined with reasonable precisions even with the simultaneous changes in sample temperature and concentration. These results indicated the feasibility of the MMI-OFC sensing cavity for the temperature-compensated RI sensing or the simultaneous measurement of the material-depended RI and the sample temperature.

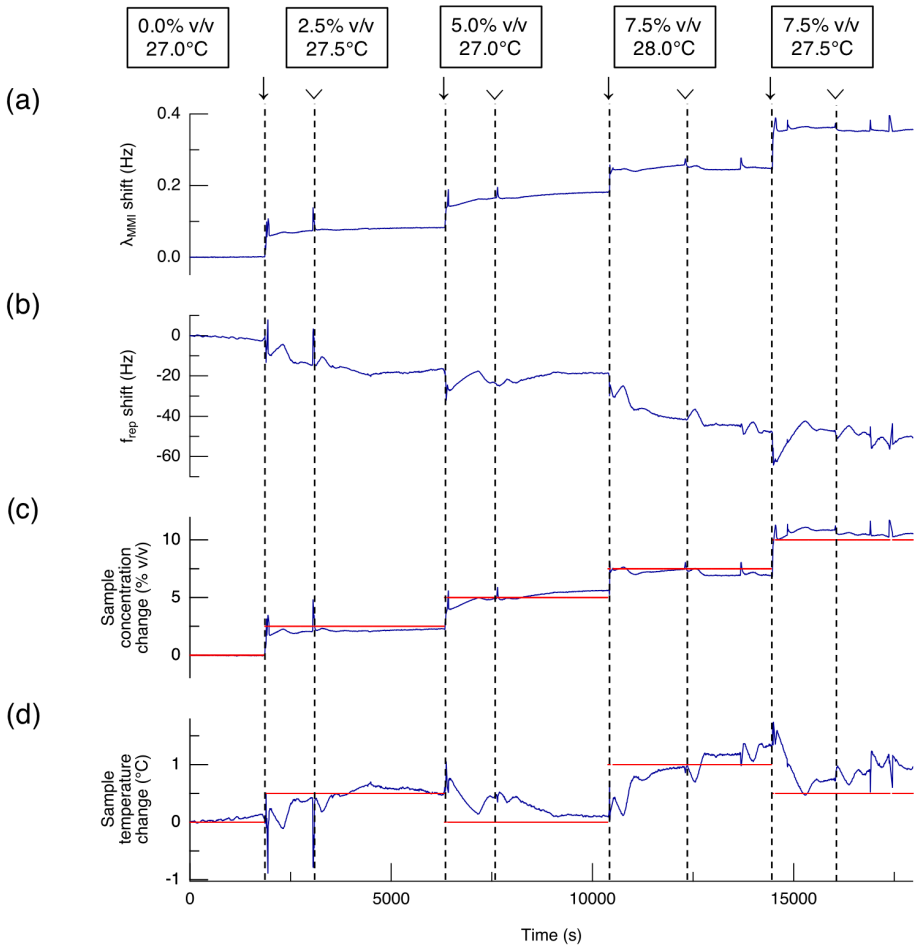

Fig. 21. Simultaneous measurement of temperature and RI-related concentration of an ethanol/water solution under the variable temperature and the variable ethanol concentration. (a) Temporal behavior of the λ_{MMI} shift. (b) Temporal behavior of f_{rep} shift. (c) Temporal behavior of the estimated sample concentration change. The red line indicates the actual concentration of the ethanol/water solution. (d) Temporal behavior of the estimated sample concentration change. The red line in Figs. 21(c) and 21(d) respectively indicate the actual concentration of the ethanol/water solution and the setting temperature of the ethanol/water solution. The arrows indicate the times at which the temperature was changed and/or the ethanol was applied. The arrow heads indicate the times at which the sample was stirred.

4.3 Discussion

In the proposed MMI-OFC sensing cavity, the RI sensing with temperature compensation was realized by observing the optical spectral shift $\Delta\lambda_{MMI}$ and the RF spectral shift Δf_{rep}. Our finding is that the material-dependent RI and the sample temperature can change both the $\Delta\lambda_{MMI}$ and Δf_{rep}, although with different slope coefficients. First, we discuss the detection mechanism to corroborate the regularity of the slope coefficient matrix in Eq. (7). The concentration of the

sample can change the RI of the sample. The temperature of the sample can change not only the RI of the sample via the thermo-optic effect but also the RI of the MMF, the length of the MMF and the diameter of the MMF via the thermo-optic effect or the thermal expansion effect. Thus, the partial derivatives of λ_{MMI} against concentration and temperature are given by,

$$\frac{\partial \lambda_{MMI}}{\partial C} = \frac{\partial \lambda_{MMI}}{\partial n_{sam}} \frac{\partial n_{sam}}{\partial C}, \tag{8}$$

$$\frac{\partial \lambda_{MMI}}{\partial T} = \frac{\partial \lambda_{MMI}}{\partial n_{sam}} \frac{\partial n_{sam}}{\partial T} + \frac{\partial \lambda_{MMI}}{\partial n_{MMF}} \frac{\partial n_{MMF}}{\partial T} + \frac{\partial \lambda_{MMI}}{\partial L_{MMF}} \frac{\partial L_{MMF}}{\partial T} + \frac{\partial \lambda_{MMI}}{\partial D_{MMF}} \frac{\partial D_{MMF}}{\partial T}. \tag{9}$$

In contrast, as shown in Eq. (3), the repetition frequency f_{rep} is a function of cavity parameters, including the geometrical length of the fiber cavity, which would be modulated by the diameter and the length of the MMF, and the RI of the fiber cavity. The repetition frequency f_{rep} is also a function of the RI of the sample because the RI-dependent wavelength shift of the MMI fiber sensor must change the optical length of the cavity via the wavelength dispersion of the cavity fiber. In the same manner as the interference wavelength λ_{MMI}, the partial derivatives of f_{rep} against concentration and temperature are given by,

$$\frac{\partial f_{rep}}{\partial C} = \frac{\partial f_{rep}}{\partial n_{sam}} \frac{\partial n_{sam}}{\partial C}, \tag{10}$$

$$\frac{\partial f_{rep}}{\partial T} = \frac{\partial f_{rep}}{\partial n_{sam}} \frac{\partial n_{sam}}{\partial T} + \frac{\partial f_{rep}}{\partial n_{MMF}} \frac{\partial n_{MMF}}{\partial T} + \frac{\partial f_{rep}}{\partial L_{MMF}} \frac{\partial L_{MMF}}{\partial T} + \frac{\partial f_{rep}}{\partial D_{MMF}} \frac{\partial D_{MMF}}{\partial T}. \tag{11}$$

Therefore, the discriminant equation of the coefficient matrix of Eq. (7) can be expressed with Eqs. (8)-(11) as follows,

$$
\begin{aligned}
D &= \frac{\partial f_{rep}}{\partial C}\frac{\partial \lambda_{MMI}}{\partial T} - \frac{\partial f_{rep}}{\partial T}\frac{\partial \lambda_{MMI}}{\partial C} \\
&= \frac{\partial n_{sam}}{\partial C}\left[\begin{array}{l}
\left(\frac{\partial f_{rep}}{\partial n_{sam}}\frac{\partial \lambda_{MMI}}{\partial n_{MMF}} - \frac{\partial f_{rep}}{\partial n_{MMF}}\frac{\partial \lambda_{MMI}}{\partial n_{sam}}\right)\frac{\partial n_{MMF}}{\partial T} \\
+\left(\frac{\partial f_{rep}}{\partial n_{sam}}\frac{\partial \lambda_{MMI}}{\partial L_{MMF}} - \frac{\partial f_{rep}}{\partial L_{MMF}}\frac{\partial \lambda_{MMI}}{\partial n_{sam}}\right)\frac{\partial L_{MMF}}{\partial T} \\
+\left(\frac{\partial f_{rep}}{\partial n_{sam}}\frac{\partial \lambda_{MMI}}{\partial D_{MMF}} - \frac{\partial f_{rep}}{\partial D_{MMF}}\frac{\partial \lambda_{MMI}}{\partial n_{sam}}\right)\frac{\partial D_{MMF}}{\partial T}
\end{array}\right].
\end{aligned}
\tag{12}
$$

According to the discriminant equation of the coefficient matrix, the importance of the detection mechanism is the presence of the temperature dependent changes of the MMI fiber sensor, *i.e.*, the RI, the geometrical length and the diameter of the MMF. Since our results indicated that the discriminant equation is not 0, in other words, the slope coefficient matrix is regular, the temperature dependent MMF change was effectively utilized for the simultaneous measurement of the RI sensing with temperature compensation using the MMI-OFC sensing cavity.

We also discuss the validity of the slope coefficients of the $\Delta\lambda_{MMI}$ and the Δf_{rep}. These slope coefficients are determined by the concentration-dependent and temperature-dependent change of sample RI n_{sam}. In general, it is known that the water/ethanol mixture shows a concentration-dependent RI change on the order of 5×10^{-4} (RIU/% v/v) [41] and temperature-dependent RI change on the order of 1×10^{-4} (RIU/℃) [43]. Therefore, these RI changes are comparable to each other, as shown in our results. In our previous research, the RI sensitivity of the MMI sensor used in this experiment was 130.3 nm/RIU [34]. From these values, the concentration-dependent and temperature-dependent $\Delta\lambda_{MMI}$ slopes are estimated as 0.061 nm/% v/v and 0.013 nm/℃, which are in reasonable agreement with the experimental data. An RI sensitivity of -6.19×10^{3} Hz/RIU was determined by RI-dependent $\Delta\lambda_{MMI}$ and the wavelength dispersion of the cavity fiber. Therefore, a concentration-dependent Δf_{rep} with slope coefficient of -2.90 Hz/% v/v was estimated, which is comparable to the experimental value (= -2.96 Hz/% v/v). In the

same manner, a temperature-dependent Δf_{rep} with slope coefficient of -10.72 Hz/℃ is calculated. This theoretical value was slightly different from the experimental value (= -20.46 Hz/ºC), this might be due to the presence of the temperature-dependent shape change of the MMI fiber sensor. Further study is required to evaluate the temperature effect on the MMI fiber sensor for the Δf_{rep} measurement, which will clarify the mechanism of the refractive index sensing with temperature compensation for more detail.

The limitation of this study is the accuracy of the temperature measurement. Although the effect of the temperature-compensated RI measurement was demonstrated in this study, the precision of the temperature measurement was still limited to 0.08 ºC. The accuracy of the temperature measurement was also limited the variation of the slope coefficients as shown in Figs. 17 and 18. To improve the accuracy of the temperature measurement, one possibility is to employ an all polarization-maintaining (PM) fiber-based OFC sensing cavity, which might be stable against environmental perturbations owing to the insensitive property of the PM fiber against the environmental perturbations. Although further studies are required for the practical application, we believe that our findings of the simultaneous measurement capability of temperature and RI-related concentration will improve the RI sensing with the MMI-OFC sensing cavity.

5. Conclusion

In this PhD thesis, to enhance the performance of the fiber RI sensing, we focused on an optical-to-electric frequency conversion function in the fiber OFC. Such the function enables a new use of OFC for a photonic RF converter. In contrast to the optical frequency measurement, the RF frequency measurement simplifies the experimental methodology and benefits from high precision, high functionality, convenience, and low cost by making use of various kinds of RF measurement apparatuses as well as commercialized frequency standard. To expand the fiber-OFC-based photonic RF converter into RI sensing, we investigated an MMI fiber sensor into a fiber OFC cavity as an intracavity RI fiber sensor, namely MMI-OFC. Most importantly, an RI-dependent shift of λ_{MMI} in the MMI-OFC cavity is converted into a shift of f_{rep} via wavelength dispersion of the cavity fiber. Such photonic RI-to-RF conversion enables f_{rep}-reading RI sensing, in which f_{rep} is the most stable photonic RF signal in various lasers.

To perform the proof of concept and improve the sensing performance of MMI-OFC, the following three topics were investigated in this PhD thesis.

(1) Refractive-index-sensing optical comb based on photonic radio-frequency conversion with intracavity multi-mode interference fiber sensor [34]

(2) Improvement of dynamic range and repeatability in a refractive-index-sensing optical comb by combining saturable-absorber-mirror mode-locking with an intracavity multimode interference fiber sensor [35]

(3) Refractive index sensing with temperature compensation by a multimode-interference fiber-based optical frequency comb sensing cavity [36]

In the first topic of this PhD thesis, we integrated an MMI fiber sensor into a fiber OFC for f_{rep}-based RI measurement for a proof of concept of RI-sensing OFC. Stable mode-locking

operation was achieved in the MMI-OFC cavity. The RI change of a liquid sample was transferred to a change in f_{rep} via multi-mode interference in the MMI fiber sensor and wavelength dispersion in the cavity fiber. The sharp spectrum and its larger spectral shift of f_{rep} signal clearly indicated the enhanced RI sensing performance compared with the broad spectrum and its smaller spectral shift of λ_{MMI} signal. Combined use of the MMI-OFC with high-precision RF measurement enables us to achieve an RI resolution of 4.88×10^{-6} RIU and an RI accuracy of 5.35×10^{-5} RIU. The concept of a precise photonic-RF-conversion OFC will expand the application scope of OFCs beyond their current use and will extend to fiber sensing, including RI sensing.

In the second topic of this PhD thesis, to improve the dynamic range and repeatability of RI sensing, we proposed use of SAM-based mode-locking, in place of NPR-based mode-locking, in MMI-OFC. The SAM-based MMI-OFC benefits from a robust mode-locking mechanism with fewer degrees of freedom, leading to the improvement of the dynamic range and repeatability of RI sensing. Improved dynamic range and repeatability were effectively demonstrated in RI sensing of the ethanol/water sample. While the RI dynamic range was significantly increased due to high robustness to the cavity disturbance caused by the MMI fiber sensor, the self-starting capability without the need for polarization control significantly improves the repeatability of frep-based RI sensing every mode-locking activation. RI sensing based on SAM-MMI-OFC will be a powerful tool for quality control of liquid products, biosensing, and gas sensing.

In the third topic of this PhD thesis, to improve the RI measurement with the MMI-OFC sensing cavity in the condition of fluctuated sample temperature, we proposed an RI sensing method with temperature compensation by using an MMI-OFC sensing cavity. Based on different sensitivity of λ_{MMI} and f_{rep} on temperature and concentration of a sample, a sample RI was extracted without the influence of sample temperature. We provided a proof-of-principle

demonstration of the proposed method by the simultaneous measurement of temperature- and concentration-dependent spectral shifts of $\Delta\lambda_{MMI}$ and Δf_{rep} slopes, realizing the simultaneous measurement of temperature and concentration of a liquid sample. We expected that the RI sensing with temperature compensation based on the MMI-OFC sensing cavity will be an effective way to precisely characterize and identify materials in various fields and opens a new aspect of OFC-based instrumentations.

Those three topics of this PhD thesis highlighted high performance in RI-sensing MMI-OFC. Benefitting from this high RI-sensing performance as well as compactness, simplicity, flexibility, noise robustness and availability inherent in fiber sensors, the proposed RI-sensing MMI-OFC [44, 45] will be a powerful tool for high-precision quality evaluation of liquid substances and characteristic evaluation of optical components. Furthermore, a combination of RI-sensing MMI-OFC with bio-sensing will expand its application scope into biomedical applications.

References

[1] S. Singh, "Refractive index measurement and its applications," Phys. Scr. **65**, 167-180 (2002).

[2] H. Suzuki, M. Sugimoto, Y. Matsui, and J. Kondo, "Effects of gold film thickness on spectrum profile and sensitivity of a multimode-optical-fiber SPR sensor," Sens. Actuator B-Chem **132**, 26–33 (2008).

[3] S. K. Chauhan, N. Punjabi, D. K. Sharma, and S. Mukherji, "A silicon nitride coated LSPR based fiber-optic probe for possible continuous monitoring of sucrose content in fruit juices," Sens. Actuator B-Chem **222**, 1240–1250 (2016).

[4] B. Sutapun, M. Tabib-Azar, and A. Kazemi, "Pd-coated elastooptic fiber optic Bragg grating sensors for multiplexed hydrogen sensing," Sens. Actuator B-Chem **60**, 27–34 (1999).

[5] J. R. Ott, M. Heuck, C. Agger, P. D. Rasmussen, and O. Bang, "Label-free and selective nonlinear fiber-optical biosensing," Opt. Express **16**, 20834–20847 (2008).

[6] D. Monzón-Hernández and J. Villatoro, "High-resolution refractive index sensing by means of a multiple-peak surface plasmon resonance optical fiber sensor," Sens. Actuator B-Chem **115**, 227–231 (2006).

[7] G. Yin, S. Lou, and H. Zou, "Refractive index sensor with asymmetrical fiber Mach–Zehnder interferometer based on concatenating single-mode abrupt taper and core-offset section," Opt. Laser Technol. **45**, 294–300 (2013).

[8] H. Fukano, T. Aiga, and S. Taue, "High-sensitivity fiber-optic refractive index sensor based on multimode interference using small-core single-mode fiber for biosensing," Jpn. J. Appl. Phys. **53**, 04EL08 (2014).

[9] S. Liu, Z. Yin, L. Zhang, L. Gao, X. Chen, and J. Cheng, "Multilongitudinal mode fiber

laser for strain measurement," Opt. Lett. **35**, 835-837 (2010).

[10] T. Guo, A. C. Wong, W. S. Liu, B. O. Guan, C. Lu, and H. Y. Tam, "Beat-frequency adjustable Er^{3+}-doped DBR fiber laser for ultrasound detection," Opt. Express **19**, 2485-2492 (2011).

[11] Y. Liang, L. Jin, L. Wang, X. Bai, L. Cheng, and B.-O. Guan, "Fiber-Laser-Based Ultrasound Sensor for Photoacoustic Imaging," Sci. Rep. **7**, 40849 (2017).

[12] T. Udem, J. Reichert, R. Holzwarth, and T. W. Hänsch, "Accurate measurement of large optical frequency differences with a mode-locked laser," Opt. Lett. **24**, 881–883 (1999).

[13] M. Niering, R. Holzwarth, J. Reichert, P. Pokasov, T. Udem, M. Weitz, T. W. Hänsch, P. Lemonde, G. Santarelli, M. Abgrall, P. Laurent, C. Salomon, and A. Clairon, "Measurement of the hydrogen 1S- 2S transition frequency by phase coherent comparison with a microwave cesium fountain clock," Phys. Rev. Lett. **84**, 5496–5499 (2000).

[14] T. Udem, R. Holzwarth, and T. W. Hänsch, "Optical frequency metrology," Nature **416**, 233–237 (2002).

[15] S. A. Diddams, L. Hollberg, and V. Mbele, "Molecular fingerprinting with the resolved modes of a femtosecond laser frequency comb," Nature **445**, 627–630 (2007).

[16] A. Asahara, A. Nishiyama, S. Yoshida, K. I. Kondo, Y. Nakajima, and K. Minoshima, "Dual-comb spectroscopy for rapid characterization of complex optical properties of solids," Opt. Lett. **41**, 4971–4974 (2016).

[17] T. Minamikawa, Y.-D. Hsieh, K. Shibuya, E. Hase, Y. Kaneoka, S. Okubo, H. Inaba, Y. Mizutani, H. Yamamoto, T. Iwata, and T. Yasui, "Dual-comb spectroscopic ellipsometry," Nat. Commun. **8**, 610 (2017).

[18] N. Kuse, A. Ozawa, and Y. Kobayashi, "Static FBG strain sensor with high resolution and large dynamic range by dual-comb spectroscopy," Opt. Express **21**, 11141–11149 (2013).

[19] I. Coddington, W. C. Swann, L. Nenadovic, and N. R. Newbury, "Rapid and precise

absolute distance measurements at long range," Nat. Photonics **3**, 351–356 (2009).

[20] P. A. Elzinga, R. J. Kneisler, F. E. Lytle, Y. Jiang, G. B. King, and N. M. Laurendeau, "Pump/probe method for fast analysis of visible spectral signatures utilizing asynchronous optical sampling," Appl. Opt. **26**, 4303–4309 (1987).

[21] Y. Takagi and S. Adachi, "Subpicosecond optical sampling spectrometer using asynchronous tunable mode-locked lasers," Rev. Sci. Instrum. **70**, 2218–2224 (1999).

[22] A. Bartels, R. Cerna, C. Kistner, A. Thoma, F. Hudert, C. Janke, and T. Dekorsy, "Ultrafast time-domain spectroscopy based on high-speed asynchronous optical sampling," Rev. Sci. Instrum. **78**, 035107 (2007).

[23] A. Abbas, Y. Guillet, J.-M. Rampnoux, P. Rigail, E. Mottay, B. Audoin, and S. Dilhaire, "Picosecond time resolved opto-acoustic imaging with 48 MHz frequency resolution," Opt. Express **22**, 7831–7843 (2014).

[24] A. Asahara and K. Minoshima, "Development of ultrafast time-resolved dual-comb spectroscopy," APL Photon. **2**, 041301 (2017).

[25] K. Minoshima and H. Matsumoto, "High-accuracy measurement of 240-m distance in an optical tunnel by use of a compact femtosecond laser," Appl. Opt. **39**, 5512–5517 (2000).

[26] K. Minoshima, K. Arai, and H. Inaba, "High-accuracy self-correction of refractive index of air using two-color interferometry of optical frequency combs," Opt. Express **19**, 26095–26105 (2011).

[27] G. Wu, M. Takahashi, K. Arai, H. Inaba, and K. Minoshima, "Extremely high-accuracy correction of air refractive index using two-colour optical frequency combs," Sci. Rep. **3**, 1894 (2013).

[28] T. Minamikawa, T. Ogura, Y. Nakajima, E. Hase, Y. Mizutani, H. Yamamoto, K. Minoshima, and T. Yasui, "Strain sensing based on strain to radio-frequency conversion of optical frequency comb," Opt. Express **26**, 9484-9491 (2018).

[29] S. Wang, P. Lu, H. Liao, L. Zhang, D. Liu, and J. Zhang, "Passively mode-locked fiber laser sensor for acoustic pressure sensing," J. Mod. Opt. **60**,1892-1897 (2013).

[30] T. Minamikawa, T. Masuoka, T. Ogura, K. Shibuya, R. Oe, E. Hase, Y. Nakajima, Y. Yamaoka, T. Mizuno, M. Yamagiwa, Y. Mizutani, H. Yamamoto, T. Iwata, K. Minoshima, and T. Yasui, "Ultrasonic wave sensing using optical-frequency-comb sensing cavity for photoacoustic imaging," OSA Continuum **2**, 439-449 (2019).

[31] Y. Jung, S. Kim, D. Lee, and K. Oh, "Compact three segmented multimode fibre modal interferometer for high sensitivity refractive-index measurement," Meas. Sci. Technol. **17**, 1129–1133 (2006).

[32] Q. Wang and G. Farrell, "All-fiber multimode-interference-based refractometer sensor: proposal and design," Opt. Lett. **31**, 317–319 (2006).

[33] S. Taue, Y. Matsumoto, H. Fukano, and K. Tsuruta, "Experimental analysis of optical fiber multimode interference structure and its application to refractive index measurement," Jpn. J. Appl. Phys. **51**, 04DG14 (2012).

[34] R. Oe, S. Taue, T. Minamikawa, K. Nagai, K. Shibuya, T. Mizuno, M. Yamagiwa, Y. Mizutani, H. Yamamoto, T. Iwata, H. Fukano, Y. Nakajima, K. Minoshima, and T. Yasui, "Refractive-index-sensing optical comb based on photonic radio-frequency conversion with intracavity multi-mode interference fiber sensor," Opt. Express **26**, 19694-19706 (2018)

[35] R. Oe, T. Minamikawa, S. Taue, T. Nakahara, H. Koresawa, T. Mizuno, M. Yamagiwa, Y. Mizutani, H. Yamamoto, T. Iwata, Y. Nakajima, K. Minoshima and T.i Yasui, "Improvement of dynamic range and repeatability in a refractive-index-sensing optical comb by combining saturable-absorber-mirror mode-locking with an intracavity multimode interference fiber sensor," Jpn. J. Appl. Phys. **58**, 060912 (2019).

[36] R. Oe, T. Minamikawa, S. Taue, H. Koresawa, T. Mizuno, M. Yamagiwa, Y. Mizutani, H.

Yamamoto, T. Iwata, and T. Yasui, "Refractive index sensing with temperature compensation by a multimode-interference fiber-based optical frequency comb sensing cavity," Opt. Express **27**, 21463-21476 (2019).

[37] A. Komarov, H. Leblond, and F. Sanchez, "Theoretical analysis of the operating regime of a passively-mode-locked fiber laser through nonlinear polarization rotation," Phys. Rev. A **72**, 063811 (2005).

[38] B. Ortaç, M. Plötner, J. Limpert, and A. Tünnermann, "Self-starting passively mode-locked chirped-pulse fiber laser," Opt. Express **15**, 16794-16799 (2007).

[39] H. Fukano, D. Watanabe, and S. Taue, "Sensitivity characteristics of multimode-interference optical-fiber temperature-sensor with solid cladding material," IEEE Sensors J. **16**, 8921-8927 (2016).

[40] J. E. Antonio-Lopez, A. Castillo-Guzman, D. A. May-Arrioja, R. Selvas-Aguilar, and P. LiKamWa, "Tunable multimode-interference bandpass fiber filter," Opt. Lett. **35**, 324-326 (2010).

[41] J. V. Herráez and R. Belda, "Refractive indices, densities and excess molar volumes of monoalcohols + water," J. Solution Chem. **35**, 1315-1328 (2006).

[42] T. Yasui, R. Ichikawa, Y.-D. Hsieh, K. Hayashi, H. Cahyadi, F. Hindle, Y. Sakaguchi, T. Iwata, Y. Mizutani, H. Yamamoto, K. Minoshima, and H. Inaba, "Adaptive sampling dual terahertz comb spectroscopy using dual free-running femtosecond lasers," Sci. Rep. **5**, 10786 (2015).

[43] A. N. Bashkatov and E. A. Genina, "Water refractive index in dependence on temperature and wavelength: a simple approximation," Proc. SPIE **5068**, 393-395 (2003).

[44] T. Nakahara, R. Oe, T. Minamikawa, S. Taue, T. Kajisa, T. Yasui, "Intra-cavity biosensing in refractive- index-sensing optical comb" in *14th Pacific Rim Conference on Lasers and Electro-Optic*, C2D_4, Aug. 3, 2020 (Aug. 3-5, 2020/online).

[45] T. Nakahara, R. Oe, T. Kajisa, S. Taue, T. Minamikawa, and T. Yasui, "Refractive-index-sensing optical comb using intra-cavity multi-mode-interference fiber sensor and its application for bio-sensing," in *OSA Optical Sensors and Sensing, Technical Digest*, JTu2A.23, June 23, 2020 (June 22-26, 2020/online).